First principles study on NASICON-based rechargeable sodium-ion batteries: Structures and diffusion in cathode, electrolyte materials and through interfaces

Bui Thi Kieu My

Doctoral Program in Nano-Science and Nano-Technology

Submitted to the Graduate School of Pure and Applied Sciences
in Partial Fulfillment of the Requirements
for the Degree of Doctor of Philosophy in Science

at the

University of Tsukuba

Abstract

For large-scale applications in battery market, sodium ion batteries attract attention as a promising candidate thanks for its high abundance and affordable price. The finding of all-solid-state batteries using solid electrolytes for advancing the safety and reliability is necessary. The all solid-state battery using 3-D NASICON-type $Na_3V_2(PO_4)_3$ (NVP) as electrode and $Na_3Zr_2Si_2PO_{12}$ (NZSP) as electrolyte is attracting attention as a high performance and low cost battery. NVP is becoming a promising electrode material by providing good stability and high ionic conductivity. Furthermore, the material can be used as both anode and cathode. Meanwhile, NZSP is well known as a high ionic conductivity electrolyte. Since NVP and NZSP have the same NASICON structure, there is a possibility to study the NVP/NZSP/NVP cell theoretically and experimentally. However, to the best of our knowledge, there is still lack of a systematic study of NVP, NZSP, as well as NVP/NZSP interface. In this dissertation, based on the first principle calculation, a systematic study of the crystal and electronic structures, and diffusion mechanism of the cathode NVP, the electrolyte NZSP, and the NVP/NZSP interface is presented. For the first time, the role of the small polaron, which forms and migrates during the movement of Na ions in NVP, is addressed.

The hybrid functional method (HSE06) and generalized gradient approximation (GGA) implemented in the Vienna ab initio simulation package are used for the calculation of bulk of NVP and NZSP, respectively. GGA is utilized for the calculation at the interface. The crystal and electronic structures and the diffusion mechanism of Na ions in the cathode NVP and electrolyte NZSP are revealed. The lattice parameters obtained are in agreement with experiments. The materials are insulators with large band-gap. In NVP, when a Na vacancy is introduced in the material, a small polaron would form around a vanadium site near the vacancy. Our calculation shows that, HSE06 is more appropriate than GGA+U in dealing with polaron problem. During diffusion, the Na vacancy movement will be accompanied by the migration of the polaron. Three most preferable diffusion pathways are addressed in NVP: two intra-layer pathways and one inter-layer pathway. The activation barriers for the intra-layer and inter-layer pathways are 353 meV and 513 meV, respectively. During diffusion in NZSP, Na should move through large bottlenecks. In this material,

three different diffusion pathways are found: two inner-chain pathways and one inter-chain pathway. The activation barriers for the inner-chain and inter-chain pathways are 230 meV and 260 meV, respectively. The diffusion in NVP and NZSP is in three dimensional. For the NVP/NZSP interface, the attachment is more preferable along *a* direction. Most bonds at the interface are saturated. The density of states of the interface exhibits the characteristic of a good interface.

Acknowledgements

The Doctoral dissertation presented here would not have been possible without the support of institutions and individuals. I would like to acknowledge the University of Tsukuba and GREEN, NIMS for providing me the scholarship and a friendly and efficient research environment.

First of all, I would like to express my sincere thanks to my supervisors: Prof. Takahisa Ohno and Prof. Susumu Okada, and my advisor: Dr. Van An Dinh. I have always wanted to say thank you to Prof. Ohno Takahisa for providing me the chance to work in a professional working environment like NIMS and giving me many valuable advices during my Master and Doctoral course. I wish to give thanks to Prof. Susumu Okada for his kindness, generous support, and helpful guidance over the Doctoral course. I am grateful to Dr. Van An Dinh for teaching me from the density functional theory, calculation techniques to the writing skill of the scientific paper. His supervision is excellent and I am with great luck to be his student.

I also give thanks to Kawada-san, the secretary of Prof. Takahisa Ohno, who always helped me complete the procedures fast, smoothly, and perfect. I want to thank my colleague, Dr. Mohammad Khazaei, for valuable discussion. Thank you all my group members in CMSU (NIMS), and in Okada lab (University of Tsukuba) for the friendly working atmosphere. I am grateful to my best friend ever, Hiep Nguyen, for always taking her time to listen and talk to me. My life would be hard without the help and funny moment of my friends: Nhi, Huong, Khine.

Last but not least, I would like to say thanks to my family for giving me love and support during the years.

Table of Contents

Chapter I: Introduction

1.1   Needs of energy storages

Electrical energy storage (EES) has made an irreplaceable contribution to the world's energy supplies, especially since important issues such as the raising of global warming, the running out of non-renewable energy sources, and the increasing of human demand for energy have become dramatic. To meet the
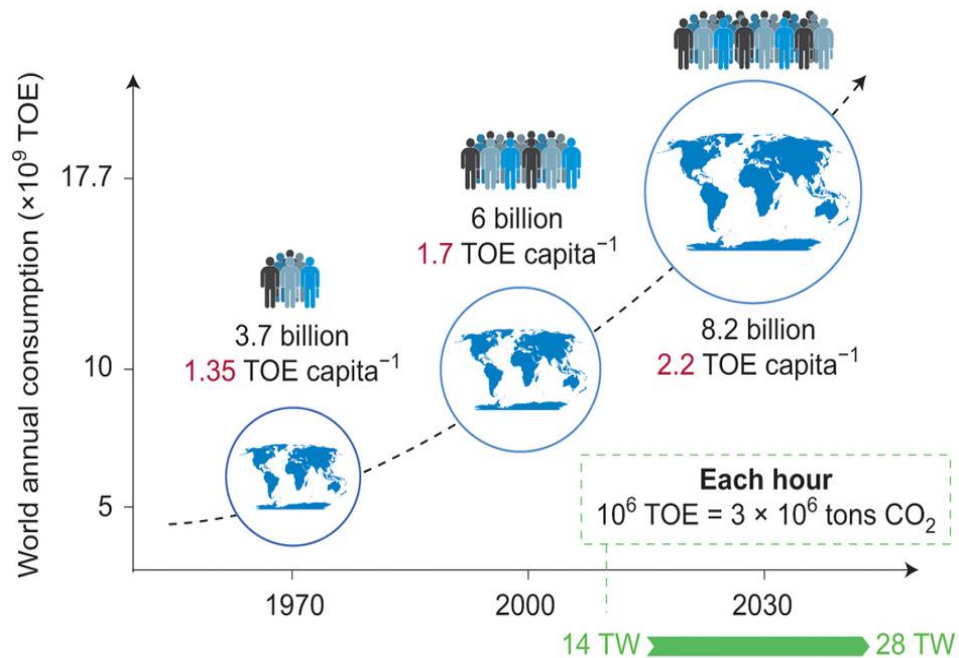

Fig. 1: Past, present and forecast of the world's energy needs up to 2050. With the changing lifestyles of an increasing number of inhabitants, our energy rate demand will double from 14 TW (2010) to 28 TW (2050). TOE = ton of oil equivalent.[1]

energy requirement, we must double our present rate of energy production of 14 TW by 2050[2]. This equates to 130,000 TWh or the equivalent of 1010 tons of oil yearly (**Fig. 1**).[1] Of course, the increase should not be accompanied with enhancing CO_2 emissions or using only finite fossil fuel resources. Some common renewable energy sources are: wind, solar, tidal, biomass and geothermal. To make the best use of these energy sources, we need good energy-storage systems. The most important criteria for applications are low cost, flexible designs, proven battery technologies, and reliable performance. There are four types of energy storage technologies for large-scale applications: mechanical, electrical, chemical, and electrochemical. As indicated in **Fig. 2**, there are several energy storage technologies that are based on batteries. In general, using electrochemical energy may have the advantage of storage such as pollution-free operation, high round-trip efficiency, flexible power, and energy characteristics to meet different grid functions, long cycle life, and low maintenance. A battery is defined as a device that can store energy in a chemical form and convert stored chemical energy into electrical energy when needed. A battery is composed of several electrochemical cells that are connected in series and/or in parallel in order to provide the required voltage and capacity, respectively. Each cell is composed of a positive and a negative electrode, where the redox reactions take place. The electrodes are separated by an electrolyte to enable ion transfer between the two electrodes. Once these electrodes are connected externally, the chemical reactions proceed in tandem at both electrodes, liberating electrons and providing the current to be tapped by the user. Batteries represent an excellent energy storage technology for the integration of renewable resources. Their compact size makes them well suited for use at distributed locations, and they can provide frequency control to reduce variations in local solar output and to mitigate output fluctuations at wind farms. Although the high cost limits market penetration, the modularity and scalability of different battery systems provide the promise of a drop in costs in the coming years.
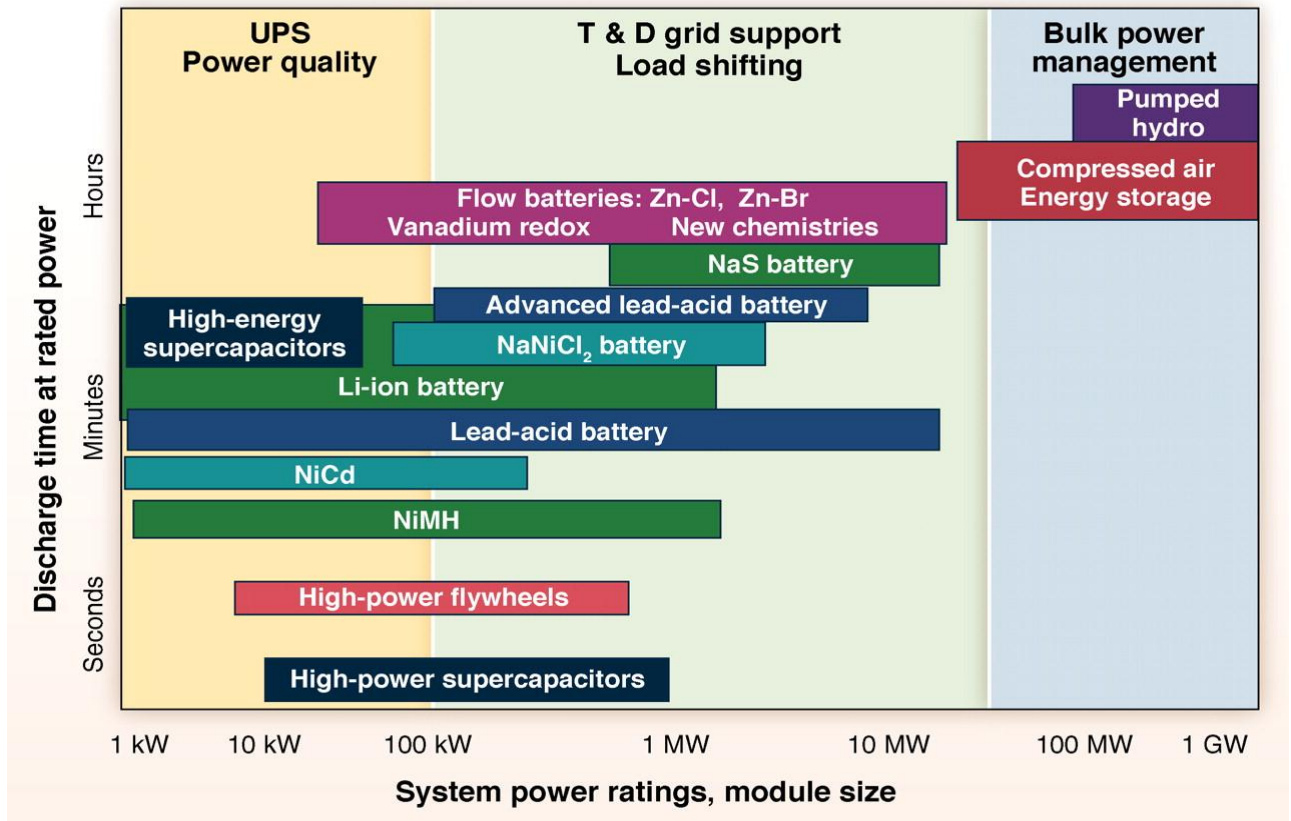
Fig. 2: Comparison of discharge time and power rating for various EES technologies. The comparisons are of a general nature because several of the technologies have broader power ratings and longer discharge times than illustrated.[3]

1.2   Rechargeable lithium ion batteries

In secondary battery family, there are various kinds of common batteries such as: flow batteries, fuel cells, lead-acid batteries, Nickel-cadmium batteries, Nickel metal hydride batteries, Li-ion batteries and so on. Among them, Li-ion batteries (LIBs) stand apart from other secondary batteries in energy density, specific energy and cell voltage as shown in **Fig. 3.** By reason of compact size, light weight, high power, and high capacity, LIBs has been dominating the commercial battery fields and their applications is getting larger and larger from small mobile devices to high power devices such as power tools, gardening tools, and electric bikes (refer to **Fig. 4**).

Fig. 3: Li ion batteries performance compare to Pb acid, Ni-Cd, Ni-MH batteries

Fig. 4: Lithium ion batteries used in everything from mobile phones to medical devices

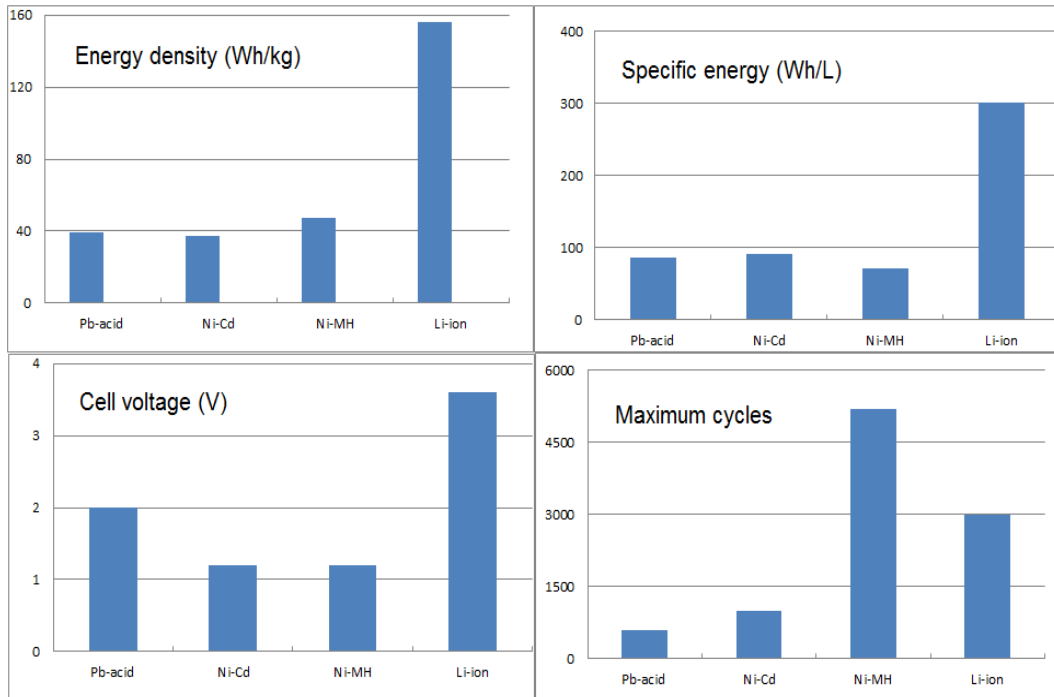**(http://www.samsungvillage.com/blog/2012/06/charge-your-knowledge-on-secondary-battery-re**

volution-in-energy.html)
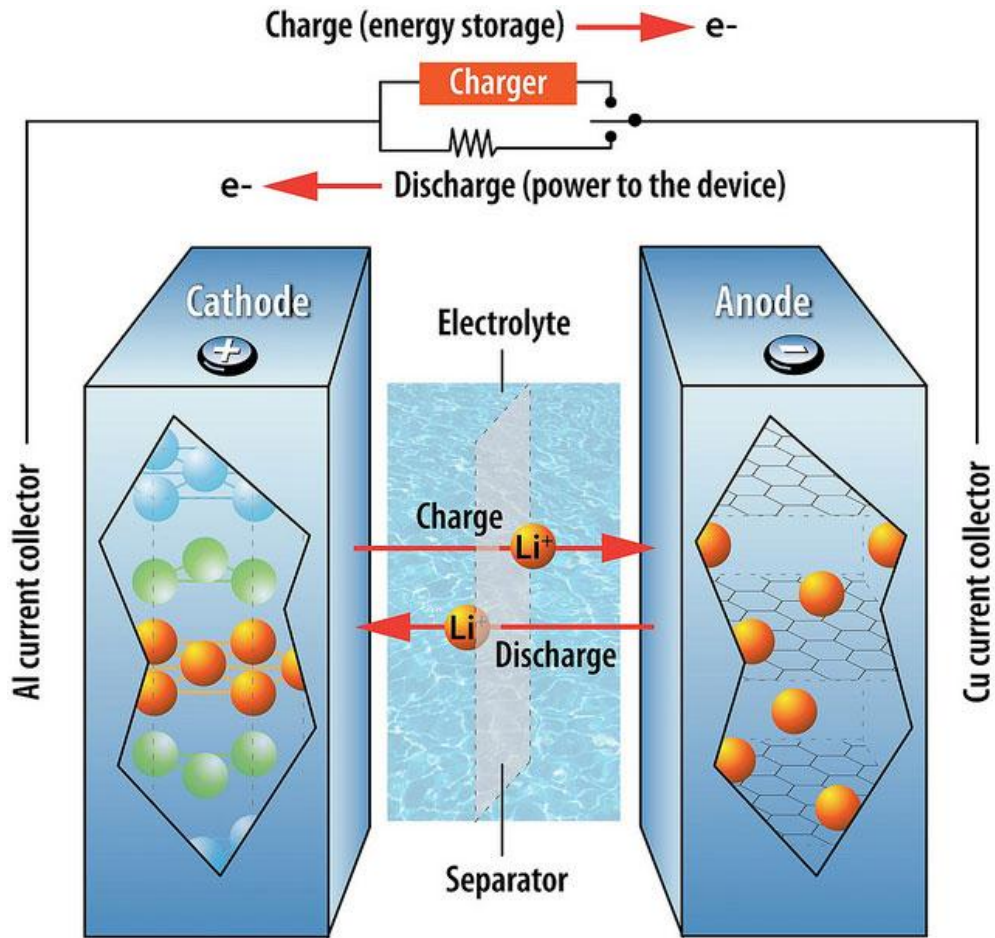
Fig. 5: Schematic of the operation of a typical Li-ion battery

(http://www.flickr.com/photos/argonne/5029455937/)

Fig. 5 illustrates the schematic operation of a typical LIB. LIB is constructed from three primary parts: anode-the source of lithium ions, cathode-the sink for the lithium ions, and electrolyte-which support the separator of ionic transport and electronic transport. During discharge, lithium ion diffuses from the anode, through electrolyte, to the cathode. Simultaneously, an electron, which generated from the reaction $Li = Li^+ + e^-$, move in the external circuit to do external work. During charge, the lithium ions and electrons travel in an opposite direction to the route they take during discharge.

On the battle of performance, LIBs are now playing the leading role with high gravimetric energy density (110-160 Wh/kg) and high voltage (3.6V).[4,5] A great deal of attention has been paid in both experimental and theoretical study of LIBs.[6–9] Nevertheless, LIBs seem not to be a strong competitor in

the battle of price because of the high price of Li and the lack of Li sources. Indeed, the abundance of Li in the Earth's crust is as small as 20ppm[10] and the Li source is unevenly distributed (mainly in South America). Hence, the search for a cheap material having comparable performance to Li is becoming an important issue.

1.3   Rechargeable sodium ion batteries

For large-scale applications where the most important factor is the cost and abundance instead of energy density, sodium-ion batteries (SIBs) seem to be better than LIBs.[11] *Table 1* provides comparison of LIBs and SIBs. Standing next to Li in the first group of periodic table, Na is the second-lightest and smallest alkali metal after Li. Na is not only the sixth most abundant element on earth crust but also a very cheap material (Price for Li carbonate: 4.11–4.49 €/kg, Na carbonate: 0.07–0.37 €/kg).[12] The diffusion of Na in SIBs can also be comparable to that of Li in LIBs.[13] Hence, extensive research about SIBs should be carried out because of such merits. Furthermore, we can also take advantage of the previous studies on LIBs since the chemical natures of Li and Na are similar. Lately, many electrode materials such as the layered structure (Na_xMO_2, M= V, Cr, Mn, Co)[14,15] and the olivine and maricite structures ($NaFePO_4$,[16] $NaV_{1-x}Cr_xPO_4F$[17]) have been widely studied. However, the heavier weight and larger ionic radius of Na ($m_{Na} = 23$ g/mol, $r_{Na} = 0.98$ Å) compared to Li ($m_{Li} = 6.9$ g/mol, $r_{Li} = 0.69$ Å)[12] make it harder to intercalate/deintercalate Na than Li, hence reduce the performance of the materials mentioned above. Therefore, it is needed to find materials where Na atoms can be easily intercalated/deintercalated.

For SIBs, a problem needed to be solved is the flammable liquid electrolytes because Na has high reactivity to moisture and oxygen causing high risk of unsafe operation. Hence, all-solid state batteries using non-flammable solid electrolytes have become usual trend in designing energy storage devices.[18,19] The benefits of using all-solid state batteries are avoiding electrolyte leakage, liquid electrolytes vaporization, and phase transition at low temperature. Also, the reliability of the all-solid

state batteries is high since they have excellent storage stability and long cycle life. In addition, all-solid state batteries may prolong battery life since the side reactions seldom happen in solid electrolyte systems. Therefore, finding appropriate materials for all-solid state battery is becoming an important issue.

Table 1: Comparison of Li batteries and Na batteries.[12]

	Li batteries	**Na batteries**
Cost (for carbonate)	$ 5,000/t	$ 150/t
Abundance (in Earth's crust)	0.0065%	2.36% (6th most abundant)
Conductivity	High	Can be comparable with Li
Normal electrode potential	-3.045 V	-2.714 V
Atomic weight	6.9 g/mol	23 g/mol
Theoretical capacity	3,829 mAh/g	1,165 mAh/g
Popularity	Widely studied	Limited studied, similar mechanism as Li

1.4   Purpose and organization of dissertation

This dissertation aims to investigate the crystal and electronic structure of cathode $Na_3V_2(PO_4)_3$, electrolyte $Na_3Zr_2Si_2PO_{12}$, and the interface; and diffusion mechanism Na ions in these materials. First, we study the crystal structure and investigate the electronic structures of the above-mentioned material. After that, we explore the formation of a small polaron which forms due to Na vacancy. We then calculate the activation energy of the elementary diffusion processes to determine the possible elementary diffusion processes. By combining the possible processes, we figure out the preferable diffusion pathways.

The dissertation contains six chapters.

o   **Chapter I** introduces the general information of Na batteries and purpose of the dissertation.

o   **Chapter II** provides the methodology which is used for the calculation. The density functional theory (GGA, GGA+U, and hybrid functional methods) for the electronic calculation are briefly introduced. The minimum energy path theory (Nudge Elastic Band) as well as the periodic supercell and pseudopotential are also given.

o   **Chapter III** presents the calculated results about geometries, electronic structure, and electrochemical properties, as well as the Na diffusion of cathode $Na_3V_2(PO_4)_3$. The results have been published in PCCP. (K. M. Bui *et al.,* Hybrid Functional Study of the NASICON-Type $Na_3V_2(PO_4)_3$: Crystal and Electronic Structures, and polaron–Na Vacancy Complex Diffusion. *Phys Chem Chem Phys*, 2015, **17**, 30433–30439).[20]

o   **Chapter IV** presents the calculated results about geometric and electronic structure of $Na_3Zr_2Si_2PO_{12}$, and diffusion of Na in the electrolyte. The results are in the submission procedure. (K. M. Bui *et al.,* Na-ion diffusion in NASICON-type solid electrolyte: a density functional study).

o   **Chapter V** presents the calculated results about geometric and electronic structure of the NVP/NZSP interface.

o   **Chapter VI** summarizes the dissertation.

Chapter II:
Calculation Method

Nowadays, the first principle calculation has been proven as a powerful tool in discovering the structural, electronic, thermodynamics properties of atom, molecules, and solids. In this chapter, we briefly present the research methodology that we need for investigating the properties of the cathode materials. The methodology of the electronic calculation such as GGA, GGA+U, and hybrid functional methods will be given. Furthermore, the periodic supercell, the pseudopotential, and the minimum energy path method for investigating the diffusion will be presented.

2.1   Density functional method

In recent times, the density functional theory has successfully shown its ability in describing ground state properties of many-body systems not only for standard bulk materials but also complex materials. In this method, the properties of many-body systems are revealed by applying functional which is spatially dependent electronic density. The name of DFT was originated from the term "functional of electronic density". In practical applications, DFT is based on approximations for the exchange-correlation potential which deals with the all effects of the electron-electron interaction.

2.1.1 Many body Schrödinger equation

In order to calculate the ground state energy of a collection of atoms, we first deal with the time independent Schrödinger equation within Born Oppenheimer approximation:

$$\hat{H}|\psi\rangle = \left(\hat{T} + \hat{U} + \hat{V}\right)|\psi\rangle = E|\psi\rangle \tag{1}$$

The kinetic energy of the electrons, $\hat{T}$, the internal potential energy $\hat{U}$, and the external potential energy, $\hat{V}$ are defined as

$$\hat{T} = \sum_{i-1}^{N} \frac{\hbar^2}{2m} \nabla_i^2 \tag{2}$$

$$\hat{U} = \sum_{i<j}^{N} \frac{e^2}{|\mathbf{r_i} - \mathbf{r_j}|} \tag{3}$$

$$\hat{V} = \sum_{i=1}^{N} v(\mathbf{r_i}) \tag{4}$$

The (total) internal electronic energy, $\hat{F}$ is defined as the composition of $\hat{T}$ and $\hat{U}$:

$$\hat{F} = \hat{T} + \hat{U} \Rightarrow \hat{H} = \hat{F} + \hat{V} \tag{5}$$

The energy of the system is given by

$$E = \langle\psi|\hat{H}|\psi\rangle = \langle\psi|\hat{T} + \hat{U} + \hat{V}|\psi\rangle$$

$$= \iint \dots \int \psi^* \left(-\sum_{i=1}^{N} \frac{\hbar^2}{2m} \nabla_i^2 + \sum_{i<j}^{N} \frac{e^2}{|\mathbf{r_i} - \mathbf{r_j}|} + \sum_{i=1}^{N} v(\mathbf{r_i})\right) \psi d\mathbf{r}_1 d\mathbf{r}_2 \dots d\mathbf{r}_N \tag{6}$$

The electron density is described as

$$n(\mathbf{r}_1) = N \iint \dots \int |\psi(\mathbf{r}_1\mathbf{r}_2 \dots \mathbf{r}_N)|^2 (d\mathbf{r}_2 \dots d\mathbf{r}_N) \tag{7}$$

It is clear that the term $\widehat{V}$ could be rewritten in a simple way, as shown below:

$$\widehat{V} = \iint \dots \int \sum_{i=1}^{N} v(\mathbf{r_i})\, \psi^* \psi\, d\mathbf{r}_1 d\mathbf{r}_2 \dots d\mathbf{r}_N = \frac{1}{N} \sum_{i=1}^{N} v(\mathbf{r}_i)\, n(\mathbf{r}_i) d(\mathbf{r}_i)$$

$$= \int v(\mathbf{r})\, n(\mathbf{r}) \tag{8}$$

However, the other terms $\widehat{T}$ and $\widehat{U}$ can not be rewritten in terms of the density as in $\widehat{V}$. By taking an expected value of $\widehat{H}$, one get

$$E = T[\psi] + U[\psi] + V[n] = F[\psi] + V[n] \tag{9}$$

In the next section, $F[\psi]$ is expressed in term of the electron density, so that the energy functional $E[n]$ can be obtained.

2.1.2   The Hohenberg-Kohn theorems[21]

2.1.2.1   The first Hohenberg-Kohn theorem.

The first theorem stated that, "For any system of interacting particles in an external potential, the density is uniquely determined".

Assume that the states are non-degenerate with the electronic density $n(r)$ in the potential $v_1(r)$ and corresponding ground state ψ_1 and energy E_1. Then we have:

$$E_1 = \langle \psi_1 | H_1 | \psi_1 \rangle = \int v_1(r) n(r) dr + \left(\psi_1, (T + U)\psi_1 \right) \tag{10}$$

Suppose that there exists a second potential $v_2(r)$, that differs from $v_1(r)$ by more than an additive constant, which gives rise to the same $n(\mathbf{r})$. The corresponding ground state and energy are ψ_2 and E_2, respectively. We get

$$E_2 = \langle \psi_2 | H_2 | \psi_2 \rangle = \int v_2(r) n(r) dr + (\psi_2, (T + U)\psi_2) \tag{11}$$

The Rayleigh-Ritz minimal principle gives

$$E_1 < \langle \psi_2 | H_1 | \psi_2 \rangle = \langle \psi_2 | H_2 | \psi_2 \rangle + \int \left(v_1(r) - v_2(r) \right) n(r) \, dr \tag{12}$$

$$E_2 < \langle \psi_1 | H_2 | \psi_1 \rangle = \langle \psi_1 | H_1 | \psi_1 \rangle + \int \left(v_2(r) - v_1(r) \right) n(r) \, dr \tag{13}$$

Summing equations (12) and (13) we obtain a contradiction

$$E_1 + E_2 < E_1 + E_2 \tag{14}$$

Thus, two different potentials cannot produce the same electron density profile $n(r)$.

2.1.2.2   The second Hohenberg-Kohn theorem

The second theorem stated that: "A universal functional for the energy $E[n]$ can be defined in terms of the density. The exact ground state is the global minimum value of this functional."   From the previous theorem, we found that the external potential is uniquely determined by the density, moreover, the external potential fixes $\hat{H}$. Thus the full many particle ground state is a unique functional of density.

The ground sate energy is given by

$$E_1 = E[n_1] = \langle \psi_1 | H_1 | \psi_1 \rangle \tag{15}$$

A different density, n_2 shall generate higher energy by the variational principle

$$E_1 = E[n_1] = \langle \psi_1 | H_1 | \psi_1 \rangle < \langle \psi_2 | H_1 | \psi_2 \rangle = E_2 \tag{16}$$

The total energy of the ground state can be obtained by minimizing the total energy of the system written as a functional of the density with respect to the density. Thus the ground state density is the

density that minimizes the energy.

2.1.3 The Kohn-Sham equations

Considering the functional $F[\tilde{n}(r)]$ of equation (5) in the form

$$F[\tilde{n}(r)] \equiv T_s[\tilde{n}(r)] + \frac{1}{2} \int \frac{\tilde{n}(r)\tilde{n}(r')}{|r - r'|} dr dr' + E_{xc}[\tilde{n}(r)] \tag{17}$$

where $T_s[\tilde{n}(r)]$ is the kinetic energy functional for non-interacting electrons, and $E_{xc}[\tilde{n}(r)]$ is the exchange-correlation energy functional.

We can rewrite the Hohenberg-Kohn variational principle for interacting electrons as

$$E_v[\tilde{n}(r)] \equiv \int v(r) n(r) dr + T_s[\tilde{n}(r)] + \frac{1}{2} \int \frac{\tilde{n}(r)\tilde{n}(r')}{|r - r'|} dr dr' + E_{xc}[\tilde{n}(r)] \geq E \tag{18}$$

The Euler-Lagrange equations for N electrons has the form

$$\delta E_v[\tilde{n}(r)] = \int \delta\tilde{n}(r) \left\{ v_{eff}(r) + \frac{\delta}{\delta\tilde{n}(r)} T_s[\tilde{n}(r)] \Big|_{\tilde{n}(r)=n(r)} - \epsilon \right\} dr = 0 \tag{19}$$

where ϵ is a Lagrange multiplier and

$$v_{eff}(r) \equiv v(r) + \int \frac{n(r')}{|r - r'|} dr' + v_{xc}(r) \tag{20}$$

$$v_{xc}(r) = \frac{\delta}{\delta\tilde{n}(r)} E_{xc}[\tilde{n}(r)]|_{\tilde{n}(r)=n(r)} \tag{21}$$

It is found that the Euler-Lagrange equation in (19) is similar to that of non-interacting particles moving in the external potential v_{eff}. Thus the density $n(r)$ can be minimized by solving the single-particle equation called Kohn-Sham equation

14

$$\left(-\frac{1}{2}\nabla^2 + v_{eff}(r) - \epsilon_j\right)\varphi_j(r) = 0 \tag{22}$$

with density $n(r)$ for an N-particle system is

$$n(r) = \sum_{j=1}^{N}\left|\varphi_j(r)\right|^2 \tag{23}$$

2.1.4 Local density approximation (LDA)

LDA[22] is the simplest and remarkably serviceable approximation for the exchange-correlation energy functional in DFT. The method based on the point of view that solid can be considered as close to the limit of the homogenous electron gas. In this method, the exchange-correlation (xc) energy functional is an integral over all space of electronic density and exchange correlation energy at each point

$$E_{xc}^{LDA} \equiv \int e_{xc}(n(r))n(r)dr \tag{24}$$

where $e_{xc}(n)$, the exchange-correlation energy per particle of a uniform gas of density n, is composed by two parts: exchange and correlation.

The exchange part is given as:[22]

$$e_x(n) \equiv -\frac{0.458}{r_s} \tag{25}$$

where r_s, the radius of a sphere containing one electron, is given by $(4\pi/3)r_s^3 = n^{-1}$

The correlation part is first described by equation[22]

$$e_c(n) \equiv -\frac{0.44}{r_s + 7.8} \tag{26}$$

15

2.1.5 Generalized gradient approximation

In order to discuss more about further accurate approximation, we first deal with the average xc hole around a given point r:

$$n_{xc}(r, r') = g(r, r') - n(r') \tag{27}$$

where $g(r, r')$ is the conditional density at r' given that one electron is at r. The average xc hole density is then written as:

$$\overline{n_{xc}}(r, r') = \int_0^1 d\lambda \, n_{xc}(r, r'; \lambda) \tag{28}$$

The publications of Harris and Jones, 1974;[23] Langreth and Pewdew, 1975;[24] Gunnarson and Lundquist, 1976 proved that the xc energy functional can be given as

$$E_{xc} = \frac{1}{2} \int dr dr' \frac{n(r)\overline{n_{xc}}(r, r')}{|r - r'|} \tag{29}$$

or

$$E_{xc} = -\frac{1}{2} \int dr dr' \overline{R_{xc}^{-1}}(r, [n(\tilde{r})]) \tag{30}$$

where

$$\overline{R_{xc}^{-1}}(r, [n(\tilde{r})]) \equiv \int dr' \frac{-\overline{n_{xc}}(r, r')}{|r - r'|} \tag{31}$$

$\tilde{n}(r)$ can then be expanded as follow since R_{xc}^{-1} is a functional of $\tilde{n}(r)$

$$n(\tilde{r}) = n + n_i \tilde{r}_i \tilde{r}_j + \cdots \tag{32}$$

where $n \equiv n(0), n_i \equiv \nabla_i n(r)|_{r=0}$, etc..

R_{xc}^{-1} can be written as

$$R_{xc}^{-1}(r) = F_0\big(n(r)\big) + F_{21}\big(n(r)\big)\nabla^2 n(r) + F_{22}\big(n(r)\big) \times \sum (\Delta_i n(r))(\Delta_i n(r)) + \cdots \qquad (33)$$

Substituting this for (30) we obtain the gradient expansion

$$E_{xc} = E_{xc}^{LDA} + \int G_2(n)(\nabla n)^2 dr + \int [G_4(n)(\nabla^2 n)^2 + \cdots] dr + \cdots \qquad (34)$$

where G_2 is a universal functional of n (Kohn and Sham, 1965). Because of the bad performance of this expansion in real systems, we can resum (32) and obtain

$$E_{xc}^0 = \int \epsilon\big(n(r)\big)n(r)dr \quad (LDA) \qquad (35)$$

$$E_{xc}^{(1)} = \int f^{(1)}(n(r), |\nabla n(r)|)n(r)dr \quad (GGA) \qquad (36)$$

$$E_{xc}^{(2)} = \int f^{(2)}(n(r), |\nabla n(r)|)\nabla^2 n(r) \qquad (37)$$

E_{xc}^0 is the LDA with one variable $x \equiv n$ while E_{xc}^0 is the so-called GGA with two variables $x \equiv n$ and $y = |\nabla n|$.

Three GGAs forms that are widely used are those proposed by Becke[25] (B88), Perdew *et al.*[26], and Perdew, Burke and Enzerhof (PBE).[27]

2.1.6   LDA+U

L(S)DA and GGA often fail to describe strong correlated system which contains transition metal or rare earth metal ions with partially filled d or f shells because of the orbital-independent potentials. In LDA+U [28–31] method, both the spin and orbital polarization are taken into account and driven by the screened on-site coulomb interactions.

The LDA+U functional is defined as

$$E^{LDA+U}[n(\mathbf{r}), \{n^\delta\}] = E^{LSDA}[n(\mathbf{r})] + E^U[\{n^\delta\}] - E_{dc}[\{n^\delta\}] \tag{38}$$

where n is the main quantum number, δ is the spin index, n^δ is the charge density for spin-δ electrons and $E^{LDA+U}[n(\mathbf{r})]$ is the standard LSDA functional. The second term of (38) is defined as:

$$\begin{aligned} E^U[\{n\}] = \frac{1}{2} \sum_{\{m\},\delta} \{ & \langle m, m''|V_{ee}|m', m'''\rangle n^\delta_{mm'} n^{-\delta}_{m''m'''} \\ & + (\langle m, m'''|V_{ee}|m', m'''\rangle - \langle m, m'''|V_{ee}|m''', m'\rangle) n^\delta_{mm'} n^\delta_{m''m'''} \} \end{aligned} \tag{39}$$

where m is the magnetic number and l is the orbital quantum number, V_{ee} are the screened Coulomb interactions among the nl electrons.

Finally, the third term of (38) is described as:

$$E_{dc}[\{n^\delta\}] = \frac{1}{2} Un(n-1) - \frac{1}{2}J[n^\uparrow(n^\uparrow - 1) + n^\downarrow(n^\downarrow - 1)] \tag{40}$$

where $n^\delta = \text{Tr}(n^\delta_{mm'})$ and $n = n^\uparrow + n^\downarrow$, U and J are screened Coulomb and exchange parameters.

2.2   Hybrid functional theory

In this method, the exchange interaction has been applied by a screened Coulomb potential. The Coulomb operators are split into short-range (SR) and long-range (LR) part:

$$\frac{1}{r} = \frac{\text{erfc}(\omega r)}{r} (\text{SR}) + \frac{\text{erf}(\omega r)}{r} (\text{LR}) \tag{41}$$

where $\text{erfc}(\omega r) = 1 - \text{erf}(\omega r)$ and ω is an adjustable parameter.

The exchange-correlation energy is defined as:

$$E_{xc}^{\text{PBE0}} = aE_x^{\text{HF}} + (1-a)E_x^{\text{PBE}} + E_c^{\text{PBE}} \tag{42}$$

where $a = 1/4$. For the exchange component:

$$E_x^{\text{PBE0}} = aE_x^{\text{HF}} + (1-a)E_x^{\text{PBE}} \tag{43}$$

and the split terms are:

$$E_x^{\text{PBE0}} = aE_x^{\text{HF,SR}}(\omega) + aE_x^{\text{HF,LR}}(\omega) + (1-a)E_x^{\text{PBE,SR}}(\omega) + E_x^{\text{PBE,LR}}(\omega)$$
$$- aE_x^{\text{PBE,LR}}(\omega) \tag{44}$$

Since the HF and PBE LR exchange parts are often small and eliminate each other, then we can neglect them and obtain.

$$E_{xc}^{\omega\text{PBEh}} = aE_x^{\text{HF,SR}}(\omega) + (1-a)E_x^{\text{PBE,SR}}(\omega) + E_x^{\text{PBE,LR}}(\omega) + E_c^{\text{PBE}} \tag{45}$$

The ωPBE hybrid, or ωPBEh are equivalent to PBE0 for $\omega = 0$ or PBE for $\omega \to \infty$. The hybrid functional method with the same screening parameter for the both of the HF and PBE parts is named as HSE06.[32]

Previous study on LiMPO$_4$[33] declared the advance of using HSE06 compare to GGA+U in predicting the binding energy. HSE06 succeeds for reproducing the peak position while GGA+U severely underestimates the binding energy obtained by experiment (refer to **Fig. 6**). More recently, Dinh *et al*[34] pointed out that GGA+U failed to describe the polaron formation in LiNiPO$_4$. In addition, the success of HSE06 in localizing the polaron is also confirmed. As illustrated in **Fig. 7**, the bound states appear in the band gap only in HSE06 calculation. Thus, a HSE06 calculation is necessary to deal with the polaron formation.
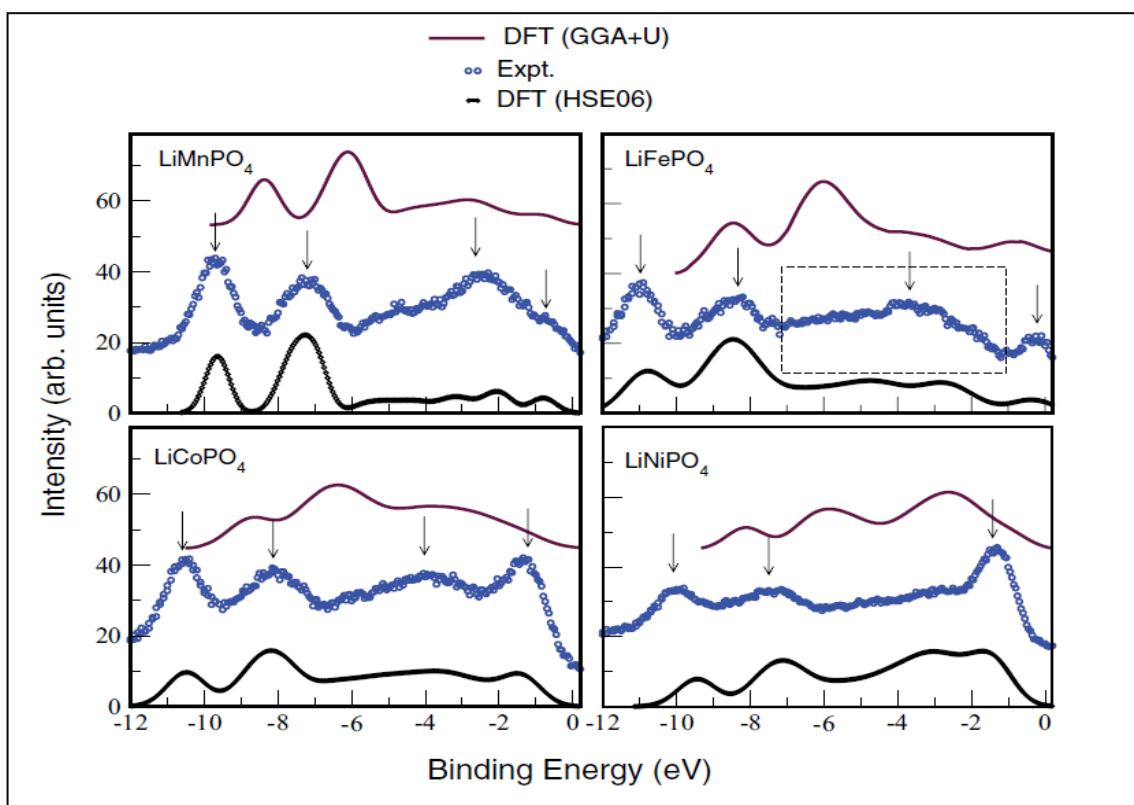
Fig. 6: A comparison of experimental XPS measurements of the binding energies to DFT calculations with two different exchange-correlation approximations. In all cases, the overall width of the spectrum and peak alignments are far better reproduced using the HSE06 methodology.[33]
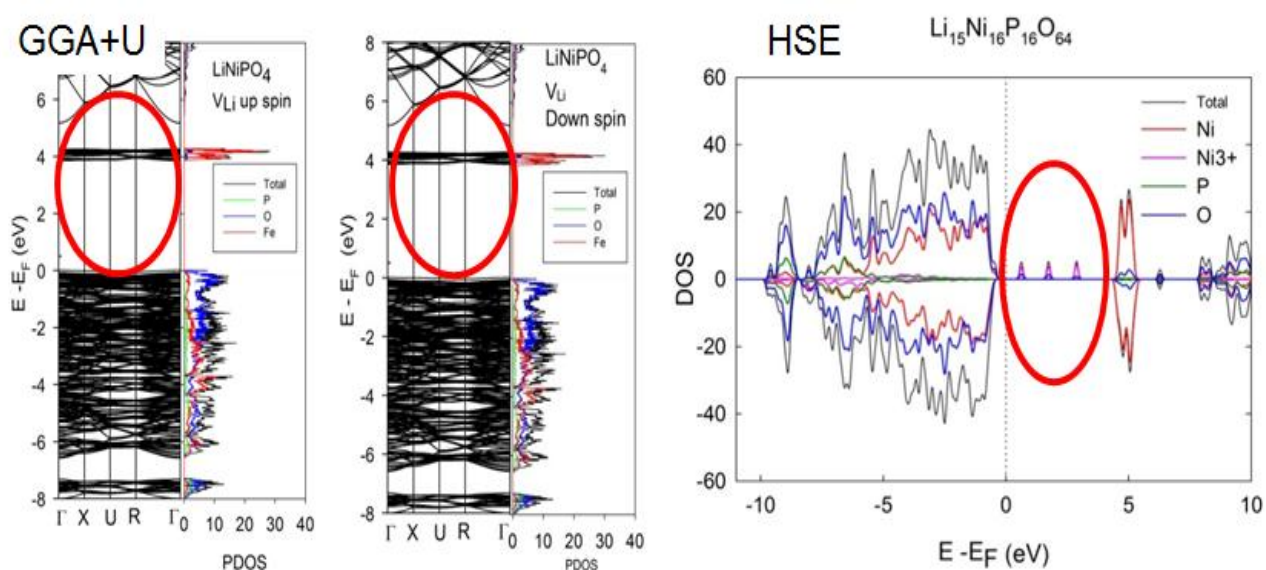

Fig. 7: DOS of LiNiPO$_4$ in vacancy structure obtained by GGA+U and HSE06.[34]

2.3   Periodic supercell

Two difficulties must be overcome: a wave function must be calculated for each of the infinite number of electrons in the system, and, since each electronic wave function extends over the entire solid, the basis set required to expand each wave function is infinite. Both problems can be surmounted by performing calculations on periodic systems and applying Bloch's theorem to the electronic wave functions. Most of the discussion in this section is based on Sec. II of ref. 35.[35]

2.3.1   Bloch's theorem

In a periodic system, electronic wave function is presented as a product of a cell-periodic part and a wavelike part,

$$\psi_i(\mathbf{r}) = \exp[i\mathbf{k} \cdot \mathbf{r}] f_i(\mathbf{r}) \tag{46}$$

The cell-periodic part can be expanded using a basis set as describe below

$$f_i(\mathbf{r}) = \sum_{\mathbf{G}} c_{i,\mathbf{G}} \exp[i\mathbf{G} \cdot \mathbf{r}] \tag{47}$$

where G is the reciprocal lattice vectors which are defined by $\boldsymbol{G} \cdot \boldsymbol{l} = 2\pi m$ ($\boldsymbol{l}$: lattice vector, m: integer). Hence, the electronic wave function is rewritten as a sum of plane waves,

$$\psi_i(\mathbf{r}) = \sum_{\mathbf{G}} c_{i,\mathbf{k}+\mathbf{G}} \exp[i(\mathbf{k} + \mathbf{G}) \cdot \mathbf{r}] \tag{48}$$

2.3.2 k-point sampling

An infinite number of k points are used to explain the infinite number of electrons in the solid, and each k point occupied a finite number of electronic states. The problem for calculating an infinite number of

electronic wave functions was changed to that for calculating a finite number of electronic wave functions at an infinite number of k points using Bloch theorem. The occupied states at each k point contribute to the electronic potential in the bulk solid so that, in principle, an infinite number of calculations are needed to compute this potential. However, the electronic wave functions at k points that are very close together will be almost identical. Hence it is possible to represent the electronic wave functions over a region of k space by the wave functions at a single k point. In this case the electronic states at only a finite number of k points are required to calculate the electronic potential and hence determine the total energy of the solid. Methods have been devised for obtaining very accurate approximations to the electronic potential and the contribution to the total energy from a filled electronic band by calculating the electronic states at special sets of k points in the Brillouin zone.[36] Using these methods, one can obtain an accurate approximation for the electronic potential and the total energy of an insulator or a semiconductor by calculating the electronic states at a very small number of k points.

2.3.3   Plane-wave basis sets

Bloch's theorem states that the electronic wave functions at each k point can be expanded in terms of a discrete plane-wave basis set. In principle, an infinite plane-wave basis set is required to expand the electronic wave functions. However, the coefficients $c_{i,\mathbf{k+G}}$ for the plane waves with small kinetic energy $(\hbar^2/2m)|\mathbf{k+G}|^2$ are typically more important than those with large kinetic energy. Thus the plane-wave basis set can be truncated to include only plane waves that have kinetic energies less than some particular cutoff energy. If a continuum of plane-wave basis states were required to expand each electronic wave function, the basis set would be infinitely large no matter how small the cutoff energy. Application of the Bloch theorem allows the electronic wave functions to be expanded in terms of a discrete set of plane waves. Introduction of an energy cutoff to the discrete plane-wave basis set produces a finite basis set.

2.4   Pseudopotential

Although Bloch's theorem states that the electronic wave functions can be expanded using a discrete set of plane waves, a plane-wave basis set is usually very poorly suited to expanding electronic wave functions because a very large number of plane waves are needed to expand the tightly bound core orbitals and to follow the rapid oscillations of the wave functions of the valence electrons in the core region. An extremely large plane-wave basis set would be required to perform an all-electron calculation, and a vast amount of computational time could be required to calculate the electronic wave functions. The pseudopotential approximation allows the electronic wave functions to be expanded using a much smaller number of plane-wave basis states. It is well known that the most of physical properties of solids depend on the valence electrons to a much greater extent than on the core electrons. The pseudopotential approximation exploits this by removing the core electrons and by replacing them and the strong ionic potential by a weaker pseudopotential that acts on a set of pseudo wave functions rather than the true valence wave functions. An ionic potential, valence wave function and the corresponding pseudopotential and pseudo wave function are illustrated schematically in **Fig. 8.** The valence wave functions oscillate rapidly in the region occupied by the core electrons due to the strong ionic potential in this region. These oscillations maintain the orthogonality between the core wave functions and the valence wave functions, which is required by the exclusion principle. The pseudopotential is constructed, ideally, so that its scattering properties or phase shifts for the pseudo wave functions are identical to the scattering properties of the ion and the core electrons for the valence wave functions, but in such a way that the pseudo wave functions have no radial nodes in the core region. In the core region, the total phase shift produced by the ion and the core electrons will be greater by π, for each node that the valence functions had in the core region, than the phase shift produced by the ion and the valence electrons. Outside the core region the two potentials are identical, and the scattering from the two potentials is indistinguishable. The phase shift produced by the ion core is different for each angular momentum component of the valence wave function, and so the scattering from the pseudopotential

23

must be angular momentum dependent. The most general form for a pseudopotential is

$$V_{NL} = \sum_{lm} |lm\rangle V_l \langle lm|$$

(49)

where $|lm\rangle$ are the spherical harmonics and V_l is the pseudopotential for angular momentum l. Acting on the electronic wave function with this operator decomposes the wave function into spherical harmonics, each of which is then multiplied by the relevant pseudopotential V_l.
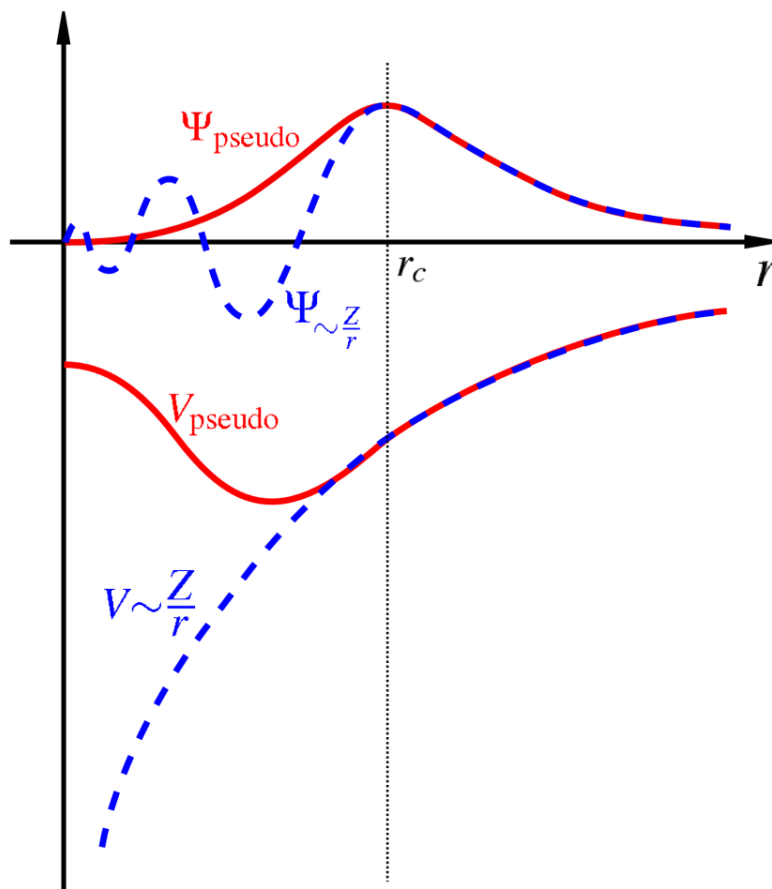

Fig. 8: . Schematic illustration of all-electron (solid lines) and pseudoelectron (dashed lines) potentials and their corresponding wave functions. The radius at which all-electron and pseudoelectron values match is designated r_c.

2.5 Nudged elastic band (NEB)

NEB is an efficient method for a finding minimum energy path (MEP) between an initial and a final state which are local minima on the potential energy surface. Every point in MEP is at an energy minimum in the directions that are perpendicular to the path. The NEB consists of a string of images connected by spring forces to keep the space equal along the reaction path. Using the force projection scheme, the NEB images can be relaxed to the MEP. There are two forces: potential forces are perpendicular to the band; and spring forces are parallel to the band as shown in

Fig. 9. The unit vector is the tangent along the path $\hat{\boldsymbol{\tau}}$ and points toward higher energy neighboring image. The NEB forces acting on image i include two components:

$$\mathbf{F}_i^{\text{NEB}} = \mathbf{F}_i^{\perp} + \mathbf{F}_i^{\text{S}\|} \tag{50}$$

where the potential force perpendicular to the band $\mathbf{F}_i^{\perp}$ is described as

$$\mathbf{F}_i^{\perp} = -\nabla(\mathbf{R}_i) + \nabla(\mathbf{R}_i) \cdot \hat{\boldsymbol{\tau}}_i \hat{\boldsymbol{\tau}}_i \tag{51}$$

and the spring force acting along the band is given as

$$\mathbf{F}_i^{\text{S}\|} = k(|\mathbf{R}_{i+1} - \mathbf{R}_i| - |\mathbf{R}_i - \mathbf{R}_{i-1}|)\hat{\boldsymbol{\tau}}_i \tag{52}$$

where k is the spring constant and $\mathbf{R}_i$ is the position of the ith image.

Finding the saddle point is important to describe the transition state within harmonic transition state theory. The saddle point can be obtained using a NEB calculation.
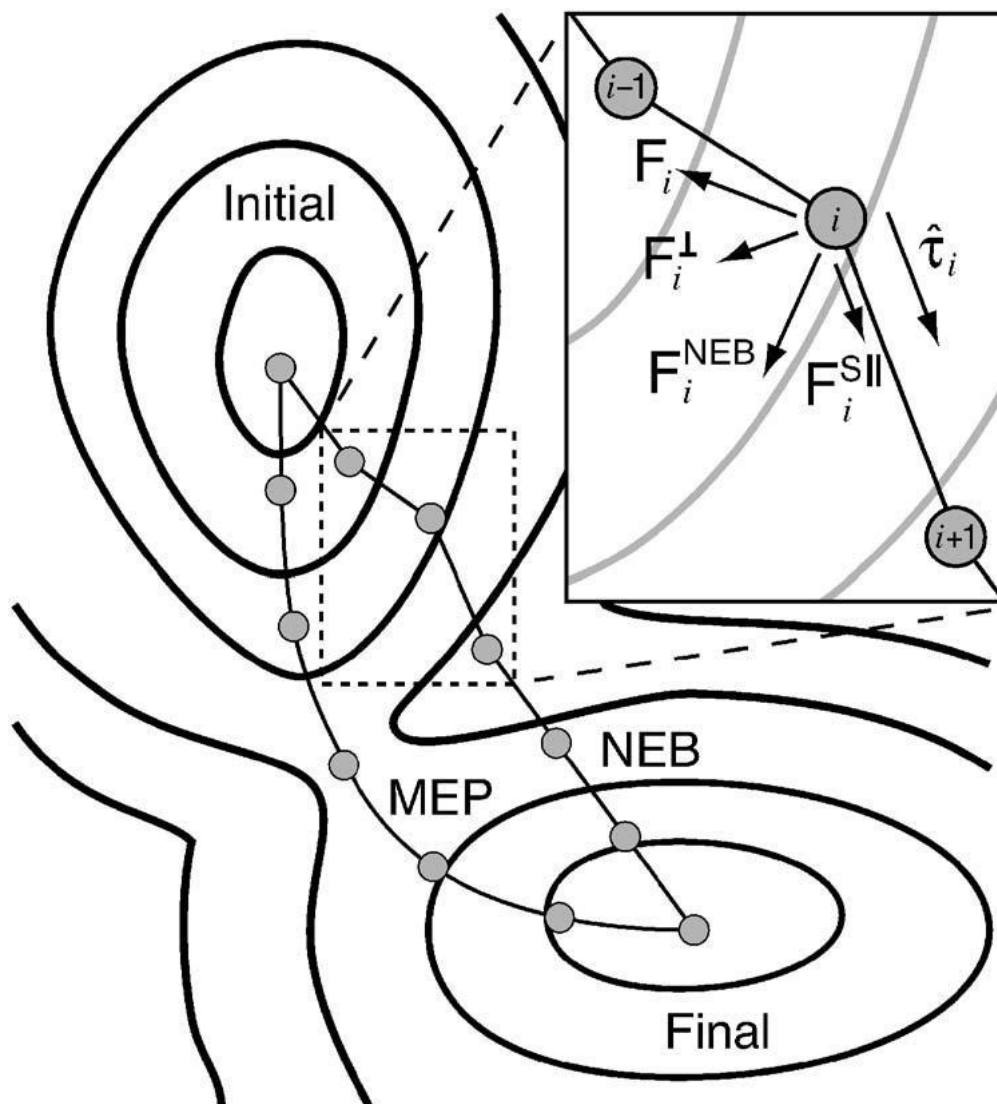
Fig. 9: Two components make up the nudged elastic band force $\mathbf{F}^{\text{NEB}}$: the spring force $\mathbf{F}_i^{\text{S}\|}$, along the tangent $\hat{\tau}_i$, and the perpendicular force due to the potential $\mathbf{F}_i^{\perp}$. The unprojected force due to the potential $\mathbf{F}_i$ is also shown in completeness.[37]

Chapter III: NASICON Na$_3$V$_2$(PO$_4$)$_3$ as a cathode material for all-solid state sodium ion batteries

The crystal and electronic structures, electrochemical properties and diffusion mechanism of the NASICON-type Na$_3$V$_2$(PO$_4$)$_3$ are investigated based on the hybrid density functional Heyd-Scuseria-Ernzerhof (HSE06). The polaron-Na vacancy complex model for revealing the diffusion mechanism is proposed for the first time in Na ion battery field. The bound polaron is found to favorably form at the first nearest V site to the Na vacancy. Consequently, the movement of Na vacancy will be accompanied by the polaron. Three preferable diffusion pathways are revealed, those are two intra-layer diffusion pathways and one inter-layer pathway. The activation barriers for the intra-layer and inter-layer pathways are 353 meV and 513 meV, respectively. For further comparison, the generalized gradient approximation with an onsite Coulomb Hubbard U (GGA+U) is also employed.

Most of the discussion in this section is taken from our published paper.[20]

3.1   Background

Recently, many experimental researches have been reported about the vanadium-based NASICON

material, namely $A_3V_2(PO_4)_3$ (A = Li,[38] Na[39–48]) whose structure is built of three dimension $V_2(PO_4)_3$ framework. The name of NASICON is the acronym for sodium (Na) Super Ionic CONductor which comes from the family of $Na_{1+x}Zr_2Si_xP_{3-x}O_{12}$ (0<x<3).[49] The NASICON structure, which is famous for its high ionic conductivity, provides large ionic sites in which lithium or sodium atoms can be inserted, hence it can be used for both LIBs and SIBs. It was proved that $A_3V_2(PO_4)_3$ can be reversibly intercalated/deintercalated. For this reason, the material is considered as a multifunctional electrode which is able to be used as not only cathode but also anode. $Na_3V_2(PO_4)_3$ (NVP) shows two voltage plateau at 3.4 V and 1.6 V, which may correspond to V^{4+}/V^{3+} and V^{3+}/V^{2+} redox couples.[43,44] **Fig. 10** shows the reversible gravimetric energy density for the first cycle of different electrochemical systems.[12] It is seen that NVP provides more energy than other related compounds. To the best of our knowledge, there is no systematic study on the Na diffusion in NVP in the literature.

Previously, it was proved that, as a Li vacancy is introduced in $LiMPO_4$ (M = Fe, Mn),[6–8,50] Li_2MSiO_4 (M = Fe, Mn, Ni) and $Li_3FePO_4CO_3$,[9] a small polaron would form at a transition metal site. Dinh *et. al.*[6] suggested a polaron-Li vacancy complex model in which the Li diffusion should be accompanied with the migration of the polaron. Later on, Bui *et. al.*[7,8,50] and Duong *et. al.*[9] successfully applied the model on Li_2MSiO_4 and $Li_3FePO_4CO_3$, respectively. According to their calculations, the GGA+U method was proved to be an appropriate method to deal well with the diffusion problem in $LiFePO_4$, $Li_3FePO_4CO_3$, and Li_2FeSiO_4 systems. Nevertheless, in $LiMnPO_4$, Li_2MnSiO_4 and Li_2NiSiO_4, the hybrid density functional HSE06 method is found to be more appropriate in addressing the polaron localization in the material. Since the Hubbard U parameter in the GGA+U method was designed to treat only the electron correlation in d states of transition metal oxides, this method may not be appropriate in the system where d states are not well localized. Fortunately, the hybrid functional could handle the polaron problem well, albeit it is a time consumer. The benefit of the hybrid functional is that it incorporates the exact Hartree-Fock (HF) and DFT to generate an exact exchange mixing, providing a more universal treatment. For this reason, the time-consuming HSE06 method was used.
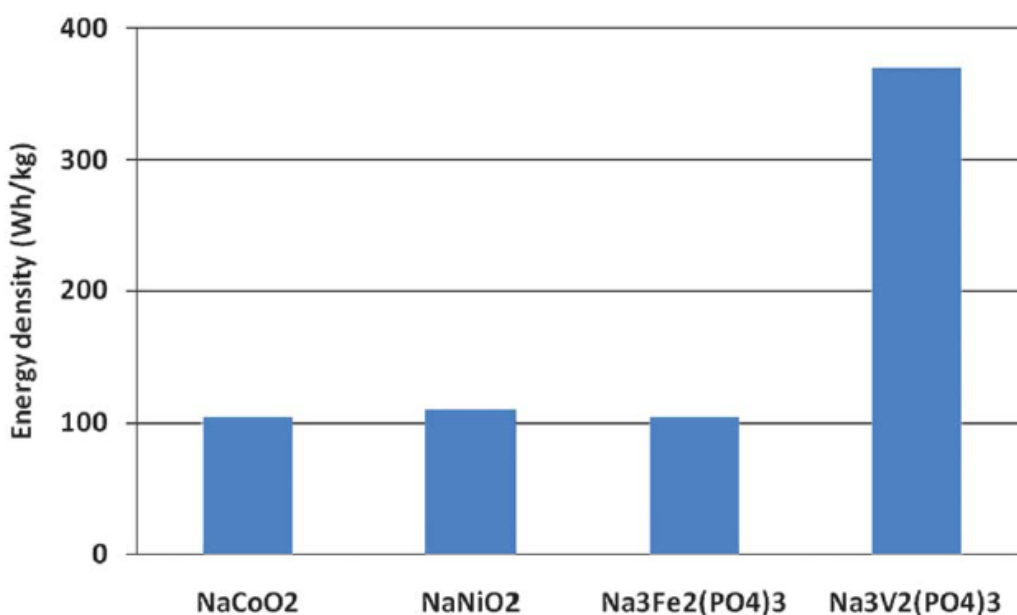
Fig. 10: Reversible gravimetric energy density for the first cycle of different cathode materials in a sodium battery with liquid organic electrolytes at room temperature[12]

3.2 Calculation scheme

Here, we investigate the crystal and electronic structure, and the diffusion in NASICON-type cathode material NVP using the HSE06 method[51] with employing the polaron-vacancy complex diffusion model. The space group of NVP is rhombohedral R$\bar{3}$c which contains of six formula units (f.u). There are 20 atoms in a f.u of NVP: 3 Na, 2 V, 3 P, and 12 O atoms. First, we find the most energetic stable structure by optimizing all possible arrangements of Na ions in the NASICON-type structure of NVP. The electronic structures of the obtained structure and the defect structure with a vacancy at the Na site were investigated. The diffusion mechanism is explored through the finding of possible elementary diffusion processes (EDP). The most preferable diffusion pathways then were revealed. The activation energies of the material along the different directions were determined by calculating the activation barriers of EDPs using the NEB[52] method.

All the calculations presented here were carried out using the Vienna ab initio simulation package (VASP).[53] A 4×4×4 k-point grid was used in GGA+U calculation. Because of the time-consuming

HSE06 method, we used the Γ-centered 2×2×2 k-point grid for the HSE06 calculation. The cut-off energy was set at 500eV for generating the plane wave basis set. Both bulk and geometry with one Na vacancy were fully optimized. The optimization calculation is converged if the residual force is less than 10^{-2} eV/Å. In addition, the result of GGA+U where U_{eff} = 4.2 eV is also presented for comparison.

3.3 Crystal structure

NVP possesses the rhombohedral NASICON structure as shown in **Fig. 11**. NASICON structure is a three-dimensional framework built of $[V_2(PO_4)_3]$ units created by corner-sharing of octahedra VO_6 and tetrahedra PO_4 along c-axis direction, and each $[V_2(PO_4)_3]$ unit is interconnected to each other through PO_4 tetrahedra. Accordingly, the hexagonal bottlenecks are formed by corner-sharing of three octahedra VO_6 and three tetrahedra PO_4. The shortest diameter of the bottleneck is 4.74 Å, which approximately equals to twice the sum of the Na^+ and O^{2-} ionic radii. During diffusion, these hexagonal bottlenecks provide large interstitial sites in which Na can easily diffuse. There are two different types of Na sites in a formula unit of $Na_3V_2(PO_4)_3$: one Na_1 site locates in an $[V_2(PO_4)_3]$ unit along the c-direction, and three Na_2 sites have the same c-coordinates with adjacent P atoms. The distribution of Na in Na sites in the primitive cell is shown in **Fig. 12.** In order to obtain the most stable $Na_3V_2(PO_4)_3$ structure, we have tested many possibilities in which six Na occupy two Na1 sites and six Na_2 sites. The Na sites are labeled from 1 to 8 as shown in **Fig. 12**. There are four groups in which two Na vacancies may locate:

-          Group 1: Two symmetry Na_2 sites at Na 1-4, 2-5, 3-6

-          Group 2: Two asymmetry Na_2 sites at Na 1-2, 1-3, 1-5, 1-6, 2-3, 2-4, 2-6, 3-4, 3-5

-          Group 3: One Na at Na_1 site, one at Na_2 site at Na 1-7, 1-8, 2-7, 2-8, 3-7, 3-8, 4-7, 4-8, 5-7, 5-8, 6-7, 6-8

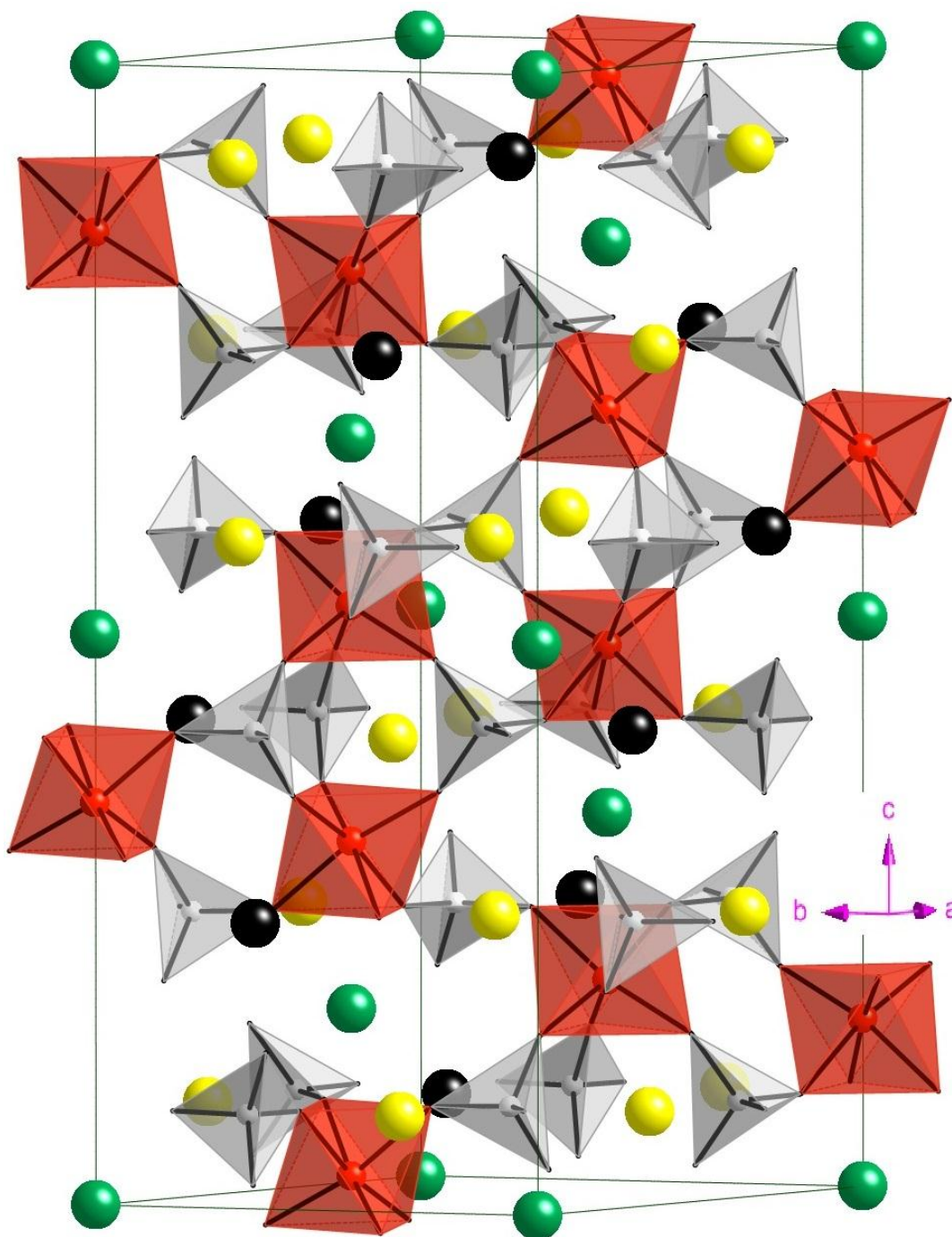-   Group 4: Two Na_1 sites at Na 7-8

Fig. 11 The crystal structure of NVP. Na at the Na$_1$ site are shown by dark green balls, Na at the Na$_2$ site by yellow balls, and the empty Na sites by black balls. The V octahedra are shown by red, and the P tetrahedra by gray.

The total energy of these four groups is shown in *Table 2*. According to *Table 2*, the most stable configuration are obtained when the Na vacancies locates at two symmetric Na_2 sites while the most unstable configuration is formed when the Na vacancies locate at two Na_1 sites. Hence, a formula unit of the most stable NVP includes one filled Na_1 site and two filled Na_2 sites. Na at the Na_2 site is likely to be more mobile than that at Na_1. This result is in accordance with the previous study[41] which reported that in NVP, the occupancy of the Na_1 site is 1.0 while that of the Na_2 site is 0.67.
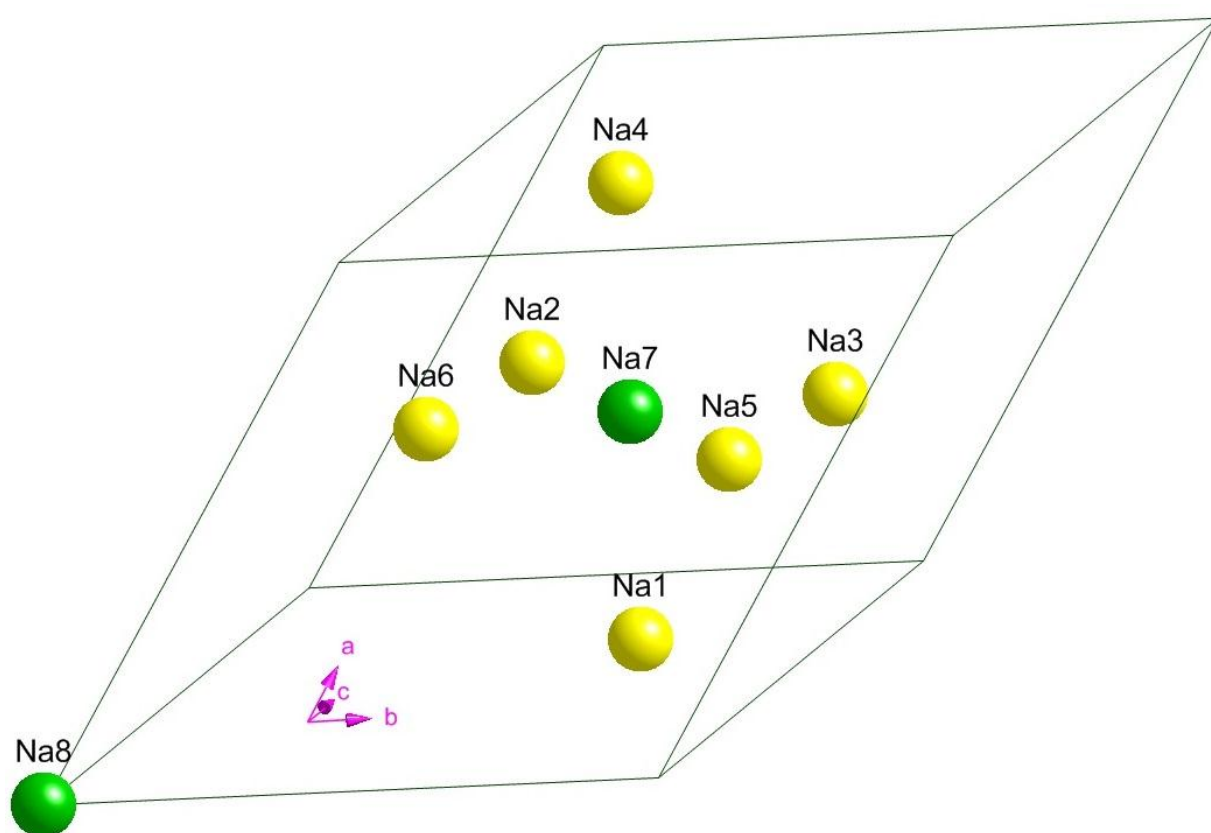

Fig. 12: Na distribution in $Na_3V_2(PO_4)_3$. Na at the Na_1 site are shown by dark green balls, Na at the Na_2 site by yellow balls.

Table 2: Total energy of NVP configurations.

Total energy (eV)	1st (most stable)	2nd	3rd	4th
Group 1	-281.83			
Group 2		-281.57		
Group 3			-281.42	
Group 4				-280.61

The geometrical parameters obtained by the HSE06 (GGA+U) method are $a = b = 8.719$ (8.826) Å, $c = 21.422$ (21.634) Å. As shown in *Table 3*, the results obtained by HSE06 and GGA+U are in good agreement with the experimental data. Our calculations show that the Na deintercalation will cause a slight contraction of lattice parameters along the a and c axes as shown in *Table 3*. All calculations in this research are spin-polarized antiferromagnetic (AFM) since the magnetic ground state of the material is AFM. Ferromagnetic arrangement (FM) is nearly as stable as AFM ($\Delta E = E_{FM} - E_{AFM} = 8$ meV/f.u.) while nonmagnetic one (NM) is the least stable state ($\Delta E = E_{NM} - E_{AFM} = 2.4$ eV/f.u.). The results of the bond distances between cations (Na, P and V) and oxygen ions in $Na_3V_2(PO_4)_3$ (NVP) and $Na_1V_2(PO_4)_3$ are summarized in *Table 4*. Referring to this table, we found that, HSE06 and GGA+U give bond lengths similar to the experiment for NVP. The Na_1 site and Na_2 site have different oxygen surrounding environments. P-O bonds remain almost constant during Na moves. This may help NVP to maintain its stability during intercalation/deintercalation. The HSE06 (GGA+U) calculation shows that average V-O bond lengths decrease from 1.99 Å (2.03 Å) to 1.91 Å (1.93 Å) during deintercalation. Such a bond-length

shrinkage is due to the change of the oxidation state of V from V^{3+} in $Na_3V_2(PO_4)_3$ to V^{4+} in $Na_1V_2(PO_4)_3$.

The deintercalation/intercalation voltage of the alkaline-based systems can be calculated by using the following formula: [13,54]

$$V = -\frac{E(A_nH) - E(A_{n-x}H) - xE(A)}{xe}$$

(53)

where E is the total energy, A is an alkali atom, A_nH is the host structure, x is the number of alkali atoms transferred and e is the absolute value of the electron charge. By using the above formula, the calculated voltage obtained by HSE06 is 3.30 V, which is in good agreement with the experimental result of 3.40 V.[44] On the other hand, the voltage of 2.51 V obtained by GGA+U is smaller than the experimental value.

Table 3: The calculated and experimental lattice parameters (Å) in $Na_3V_2(PO_4)_3$ and $Na_1V_2(PO_4)_3$.

	a,b (Å)	c (Å)
$Na_3V_2(PO_4)_3$	8.682 (Exp.)[39]	21.712
	8.719 (HSE06)	21.422
	8.826 (GGA+U)	21.634
$Na_1V_2(PO_4)_3$	8.427 (HSE06),	21.403
	8.557 (GGA+U)	21.529

Table 4: The bond distances (Å) of Na₁-O, Na₂-O, P-O, and V-O in Na₃V₂(PO₄)₃ and Na₁V₂(PO₄)₃. The experimental values are extracted from the suggested experimental geometrical structure

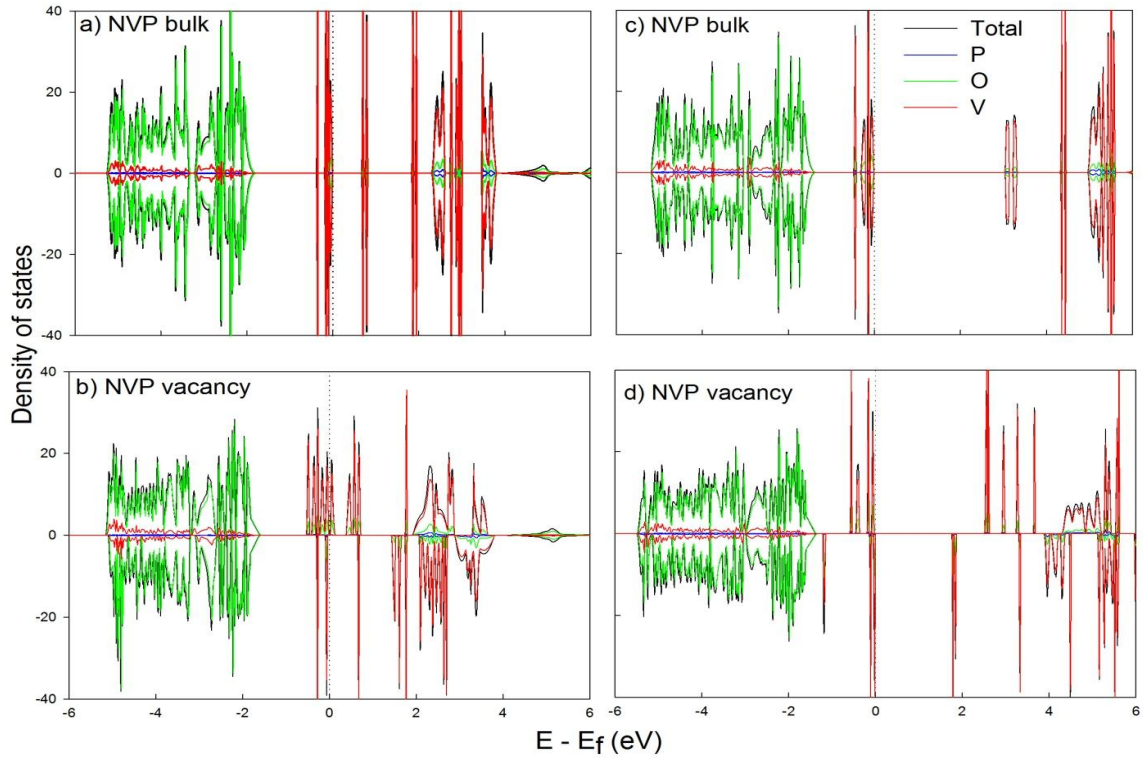|	Na₃V₂(PO₄)₃			Na₁V₂(PO₄)₃	
	Exp.[39]	Calc.		Calc.	
		HSE06	GGA+U	HSE06	GGA+U
Na₁-O (Å)	6×2.40	2×2.38 2×2.39 2×2.47	2×2.40 2×2.41 2×2.49	2×2.42 2×2.43 2×2.49	2×2.49 2×2.50 2×2.51
Na₂-O (Å)	2×2.39 2×2.43 2×2.59	2×2.39 2×2.41 2×2.49	2×2.41 2×2.43 2×2.52		
P-O (Å)	2×1.53 2×1.57	2×1.53 2×1.55	2×1.54 2×1.56	1.52 1.52 1.53 1.56	1.55 1.56 1.56 1.57
V-O (Å)	3×1.94 3×2.04	3×1.94 3×2.04	3×1.99 3×2.07	1.82 1.88 1.90 1.91 1.96 1.96	1.88 1.90 1.91 1.96 1.97 1.97

3.4 Electronic structure

Fig. 13: The antiferromagnetic DOS for the bulk and vacancy of NVP obtained by (a,b)

GGA+U   and (c,d) HSE06   methods.

Fig. 13 illustrates the spin-polarized density of states (DOS) of the bulk NVP and the NVP with defect. The projected DOS calculated by GGA+U and HSE06 of the $3d$-state of V atoms and the $2p$-state of P and O atoms are also presented. As seen from the projected DOS, the states at low energy regions are mainly contributed by $2p$-states of O atoms while those at high energy regions are dominated by $3d$-states of V atoms. The HSE06 method gives the larger band gap ($Eg_{HSE06} = 3.25eV$) than GGA+U ($Eg_{GGA+U} = 0.77eV$). As of such band gap range, the material can be considered as a semiconductor.

3.5   Polaron Formation

When a vacancy is introduced in the material, one of the V atoms would change its oxidation state from V^{3+} to V^{4+}, resulting in the formation of a small polaron. In DOS of GGA+U, the spin-polarized picture appears but it is hard to recognize if the bound states form in the band gap. For the NVP bulk, both methods generated the same local magnetic moment of V^{3+} (1.92 μ_B). The change of the calculated local magnetic moment of a V ion near the Na vacancy from 1.92 μ_B to 1.04 μ_B in HSE06 calculation implies that V ion at that site change its oxidation to +4. On the contrary, the local magnetic moment of 1.64 μ_B by GGA+U suggests that GGA+U fails for this case. The V-O bond length in NVP with defect is given in *Table 5*. The shrinkage of V-O bonds when the oxidation state of V changed from 3+ to 4+ was not observed in GGA+U calculation. The charge in GGA+U is not well localized, hence the formation of polaron at V-site is not well described. The HSE06 results show the two important evidences for the presence of the polaron, that is, the appearance of the bound states and the lattice distortions. We can see the bound states in the band-gap in DOS of the defect NVP. As seen from *Table 5*, the V-O bonds contract from 2.00 Å to 1.92 Å as a consequence of the change in the oxidation state of V from V^{3+} to V^{4+}. In short, the HSE06 functional is suitable to deal with polaron formation, whereas GGA+U is unfulfilled in describing the polaron formation in this material. Therefore, it is necessary to use the time-consuming HSE06 to deal with polaron problem in this material.

Table 6 summarizes distances between the Na-sites and its four nearest V sites. The Na_1 site and Na_2 site have different V surrounded environments. The bound polaron is found to be the most favorable at the first nearest V site.

Table 5. Vi – Oj (i = 1-4, j = 1-6) indicates the bond distance (Å) in the NVP with one vacancy. The V atoms indexed by i = 1, 3, 4 are with 3+ oxidation; i = 2 is with 4+ oxidation. The parameters are calculated by the HSE06 (GGA+U) method.

Vi – Oj (Å)	Average	$j = 1$	$j = 2$	$j = 3$	$j = 4$	$j = 5$	$j = 6$
$i = 1$	1.99 (2.00)	1.94 (1.92)	1.97 (1.98)	1.97 (2.01)	1.97 (2.00)	2.03 (2.04)	2.03 (2.07)
$i = 2$	1.92 (2.00)	1.81 (1.91)	1.91 (1.96)	2.00 (2.04)	1.91 (2.01)	1.93 (2.03)	1.98 (2.07)
$i = 3$	2.00 (2.03)	1.93 (1.96)	1.93 (1.96)	2.00 (2.01)	2.00 (2.05)	2.02 (2.06)	2.09 (2.14)
$i = 4$	2.02 (2.03)	1.93 (1.92)	1.97 (1.98)	2.05 (2.03)	2.02 (2.05)	2.06 (2.09)	2.10 (2.12)

Table 6. Distances (Å) from Na_1 and Na_2 sites to the nearest V sites in the bulk of NVP. Results are obtained by the HSE06 (GGA+U) method.

Site	1NN (Å)	2NN (Å)	3NN (Å)	4NN (Å)
Na_1	3.214 (3.154)	3.214 (3.154)	4.963 (5.089)	4.963 (5.089)
Na_2	3.077 (3.095)	3.140 (3.159)	3.877 (3.943)	3.897 (3.962)

3.6   Diffusion mechanism

As a Na vacancy diffuses, a polaron would simultaneously migrate with the Na vacancy. Therefore, the Na diffusion should be treated as diffusion of the polaron-Na vacancy complex.[6] From the previous studies, it can be seen that, depending on the system, the diffusion of the polaron-Li vacancy complex[6,8,9] can be processed in one-, two- or quasi-three dimensions. In NVP, the polaron-Na vacancy diffusion is in three dimensions as described below.

In NVP, three different diffusion pathways are available: two intra-layer pathways (Pathway 1 and Pathway 2) and one inter-layer pathway (Pathway 3). First, we reveal the diffusion along pathways inside of a Na layer. Let us index the sites where the Na vacancy passes through along Pathway 1 as I (I= A, B, C, and D). The site of the bound polaron accompanied with Na vacancy at I-site is indexed by V_I. Because Na vacancies at C and D are accompanied with the same polaron, the site of this polaron

will be indexed as V_{CD}. Thus, when Na vacancy goes through the *I* site, the accompanied polaron will migrate through the V_I site. There are four elementary processes in Pathway 1, those are, two crossing processes C_1 and C_2, one parallel process P and one single diffusion process S as described in **Fig. 14.** Here, the term "parallel" indicates that the moving direction of the Na vacancy and that of its accompanied polaron are parallel as shown in **Fig. 14**, while the term "crossing" indicates the opposite situation. Furthermore, the process in which the polaron stays on the same site during Na vacancy diffuses is called as a single process. Na vacancy moves along the *b*-direction in processes P and C_1, and along the *a*-direction in processes S and C_2, as illustrated in **Fig. 15**. Elementary process P is the process in which Na vacancy moves from A to B, while the polaron migrates from V_A to V_B. Process C_1 describes the motion of a Na vacancy from B to C, and the accompanying migration of its polaron from V_B to V_{CD}. In S process, when a Na vacancy diffuses from C to D, there is no polaron hopping since the Na vacancies at C and D have the same accompanied polaron. C_2 describes the diffusion
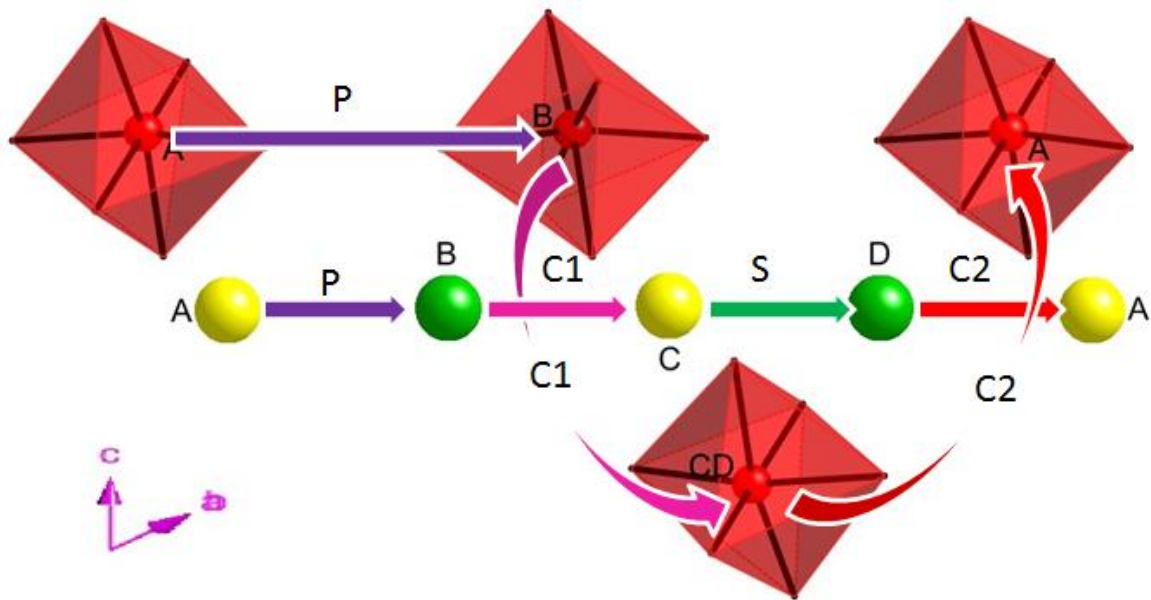

Fig. 14: Schematic of Pathway 1, polyhedral model. The purple, pink, green and red arrows represent the path of the P, C_1, S and C_2 processes, respectively.
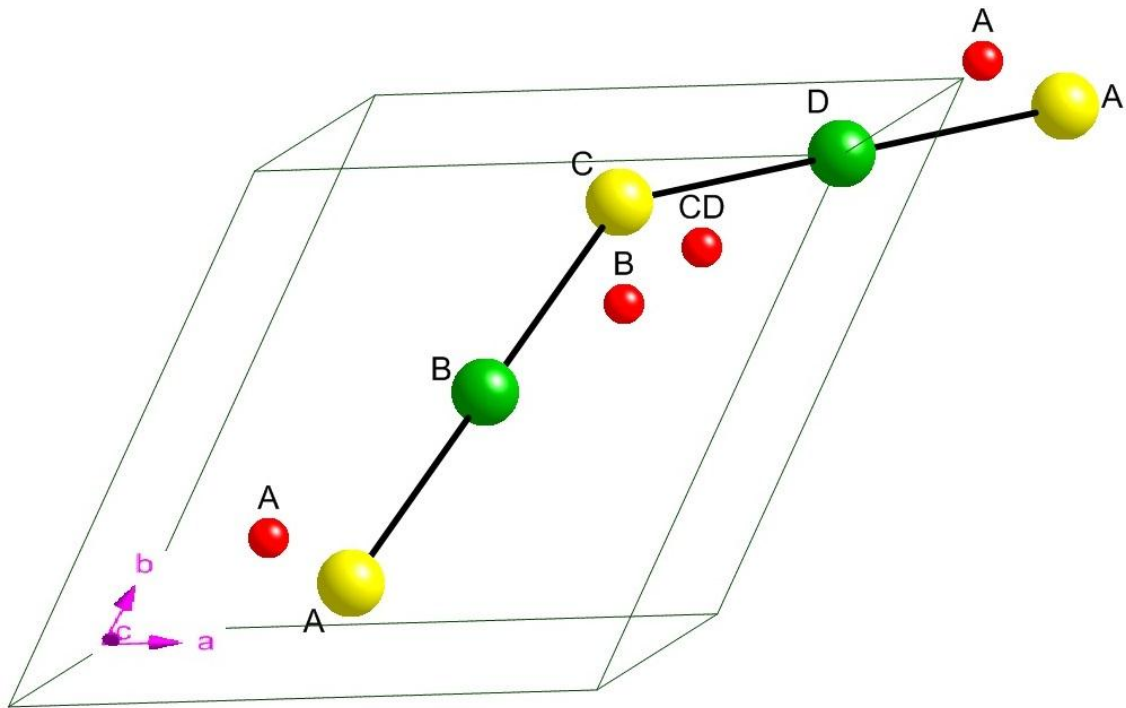
Fig. 15: Schematic of Pathway 1, ball and stick model in the *c*-direction view.

process of a Na vacancy from D to A, while its polaron from V_{CD} to V_A. If vacancy forms at the Na_2 site (say A, C), there is no severe change in the surrounding environment. On the contrary, vacancy at the Na_1 site, (say B) would attract Na at C to come closer and also give rise to some slight change in the location of the other Na ions in the cell. Therefore, the diffusion distance of the path connecting B with C, *i.e* process C_1, is as small as 2.5 Å, leading to the very low activation barrier of 137 meV. The activation barriers for P, S and C_2 processes are 283 meV, 288 meV, 353 meV, respectively. The overall activation barrier for this pathway gains 353 meV, as described in **Fig. 16**.

The diffusion mechanism and activation barrier of the polaron-Na vacancy complex in Pathway 2 is similar to that in Pathway1. While Pathway 1 proceeds in the (112) plane, Pathway 2 crosses Pathway 1 and takes place in the (121) plane as described in **Fig.17** and **Fig. 18**. **Fig. 19** depicts the trajectory of the diffusion in Pathway 1 and 2. As we described before in the structural properties part, the Na

41

vacancy has to diffuse through the hexagonal bottleneck of ZrO_6 octahedra and PO_4 tetrahedra in every elementary process. Furthermore, the diffusion in Pathway 1 and. 2 always takes place from the Na_1 site to the Na_2 site and move along parabolic-liked trajectory. Besides, we also investigate the route in which Na does not move through the hexagonal bottleneck. In this case, it is the direct Na_2 site to Na_2 site diffusion, particularly from A (or C) to the nearest Na_2 site. Since there is no large enough space for Na to diffuse, Na has to climb a barrier of energy of 1.2 eV. Because of such high barrier, this route is not a preferable pathway. Consequently, the diffusion of Na inside of a Na layer preferably happens along Pathway1 and Pathway 2.
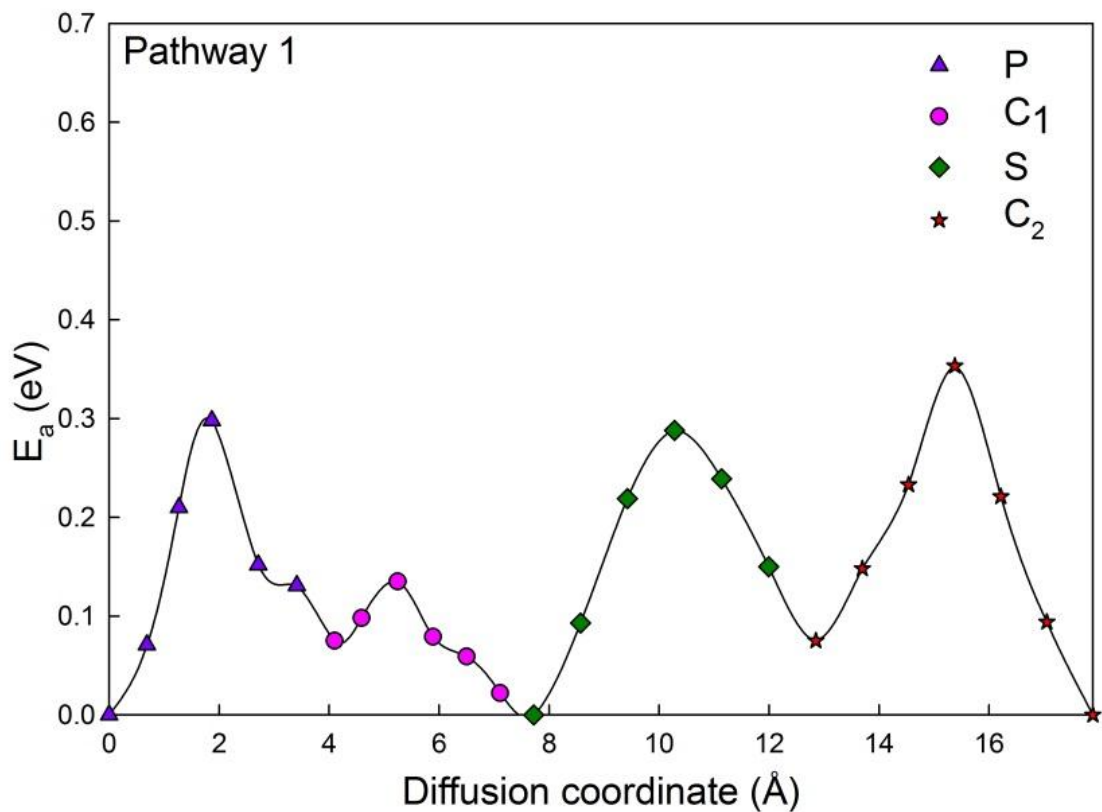
Fig. 16: Activation energies of the polaron-Na vacancy diffusion in NVP along Pathway 1. The purple circles, pink crosses, green diamonds and red stars represent the activation energy profile of the P, C_1, S and C_2 elementary diffusion processes, respectively.
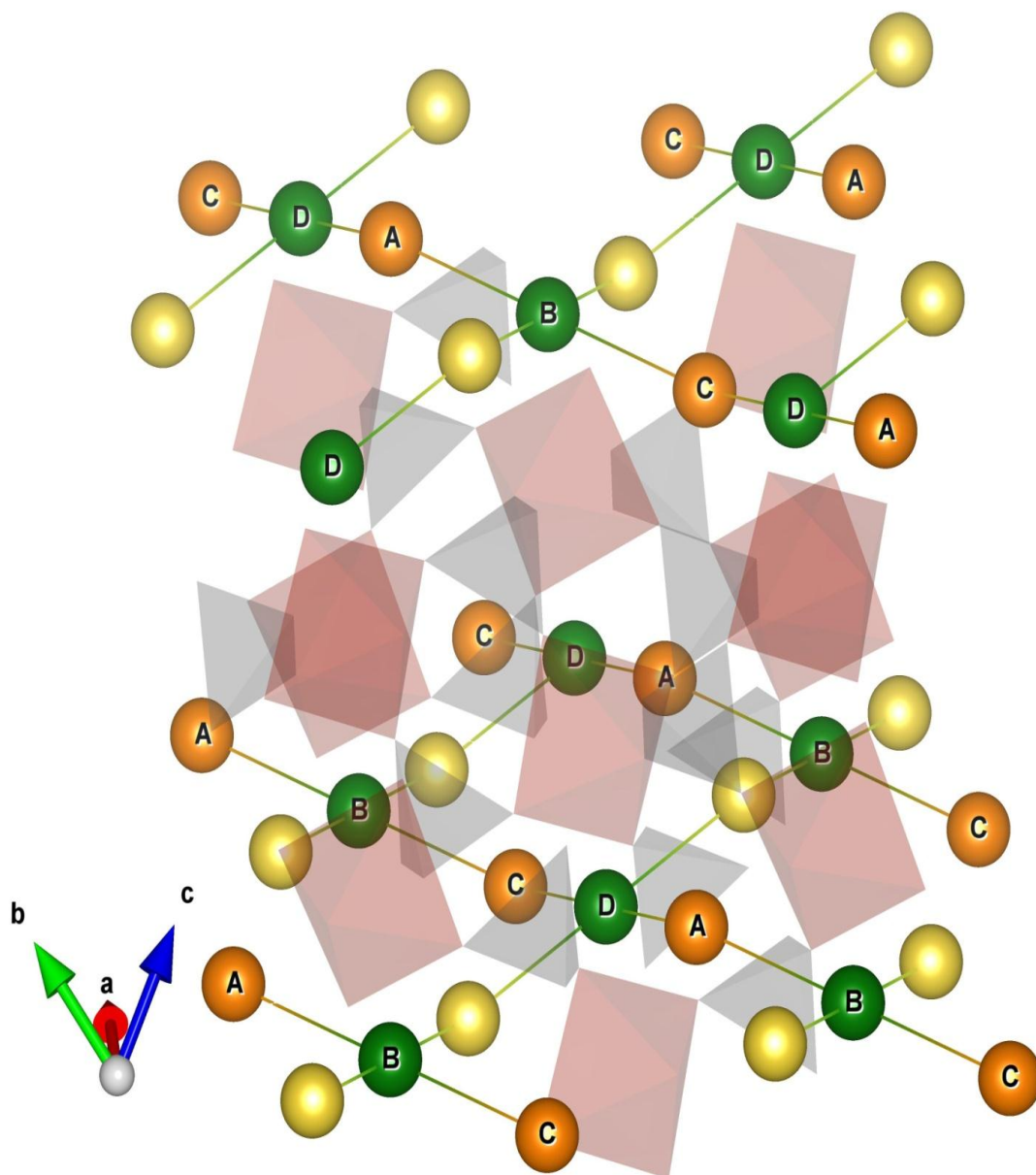
Fig. 17: Schematic of Pathway 1 and 2. The orange-green lines that connect orange Na balls and green Na balls represent for Pathway 1, and the yellow-green lines that connect yellow Na balls and green Na balls represent for Pathway 2.
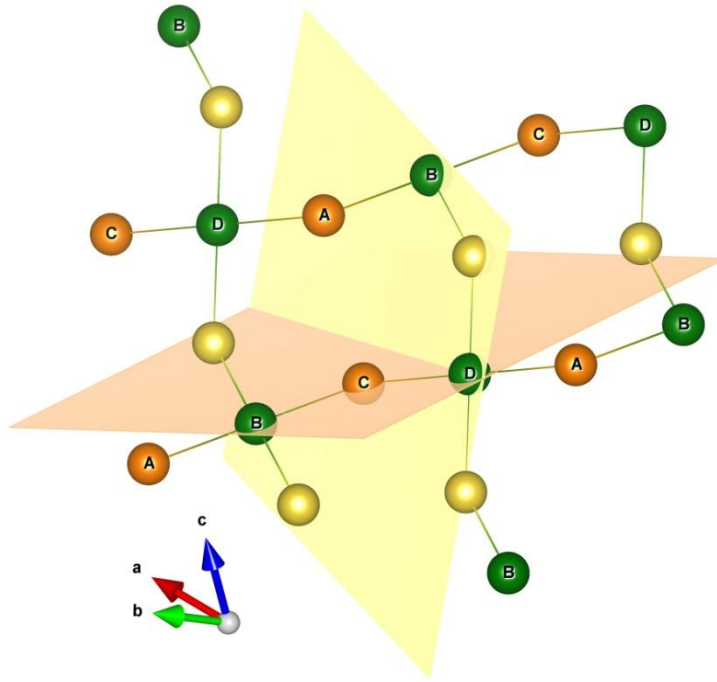
Fig. 18: **Schematic of Pathway 1 and 2. The orange plane is in the (112) plane, the yellow**
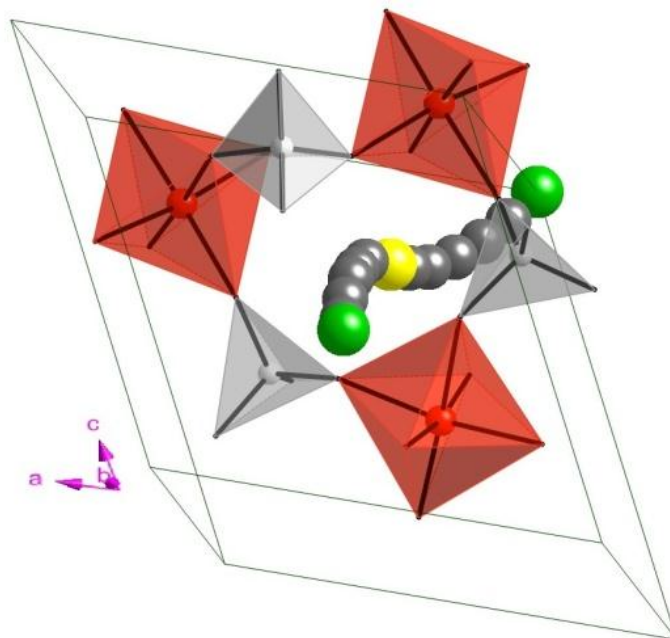
plane is in (121) plane.

Fig. 19: **Diffusion route through hexagonal bottlenecks. The deep grey ball is the transition Na.**

Next, we investigate the diffusion between two adjacent Na layers. Pathway 3 shown in **Fig. 20** is one of that called the inter-layer pathways because it connects the Na layers. In $Na_3V_2(PO_4)_3$ structure, there are two empty Na sites, named as vc_1 and vc_2. These empty sites lie in the space between two adjacent Na layers, which Na could pass through during diffusion from a Na layer to its adjacent layer as shown in **Fig. 20**. To reveal which diffusion path is the most preferred, we do the NEB calculation by choosing B and D as an initial and final position of Na vacancy, respectively; and create replicates (intermediate images) using the linear interpolation. There are two ways along which the diffusion may take place: one passes through vc_1 and the other through vc_2. According to **Fig. 21**, the calculated
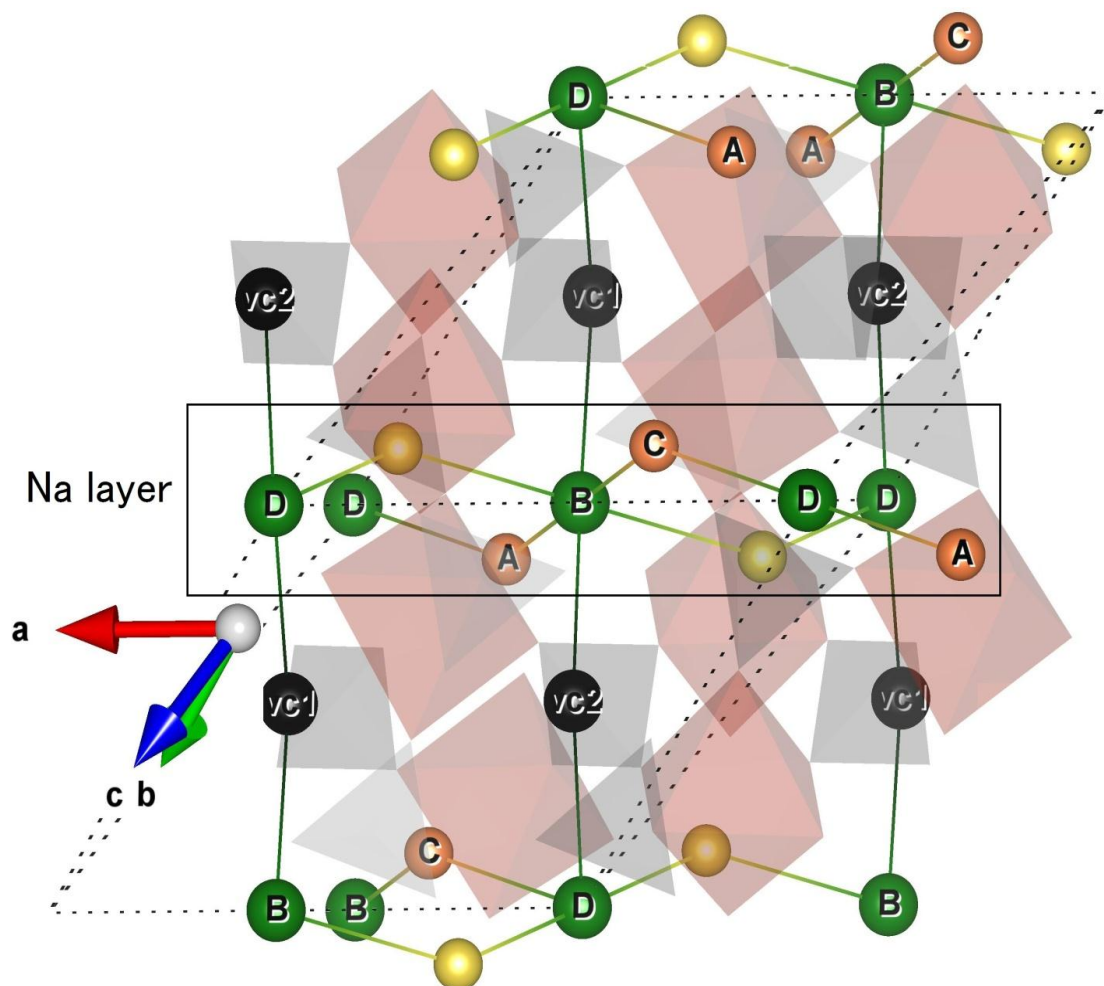

Fig. 20: Schematic of Pathway 1, 2 and 3. The black-green lines that connect Na at the Na$_1$ site and the Na vacancy represent for Pathway 3.
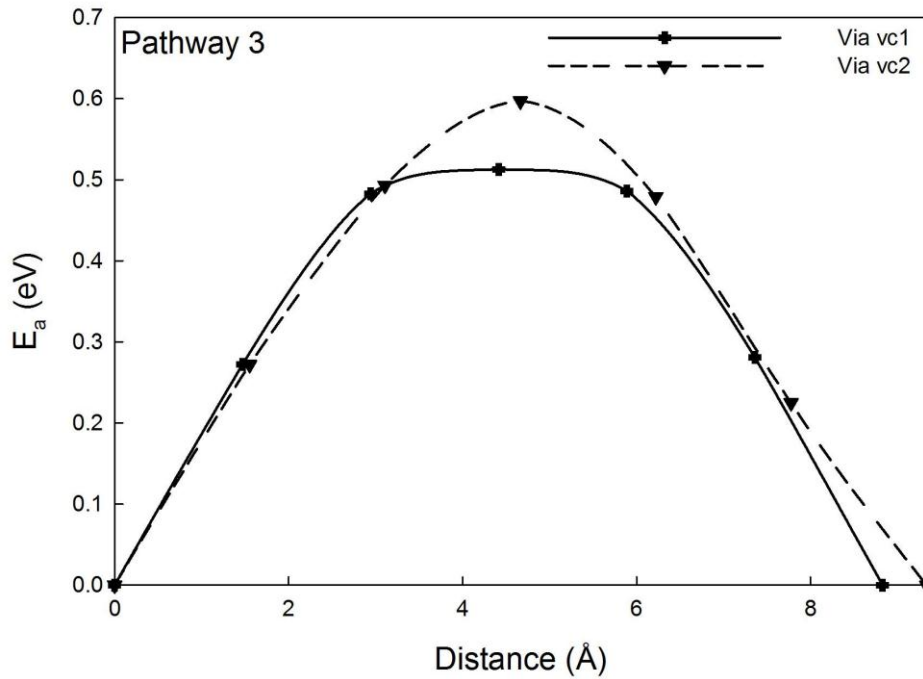
45

Fig. 21 Activation energies of the polaron-Na vacancy diffusion in NVP along Pathway 3. The solid curve represents for the diffusion process through vc1 while the dash curves represents for that through vc2.

activation energies of the diffusion processes via vc_1 and vc_2 are 513 meV and 597 meV, respectively. This means that the vacancy may prefer to diffuse through layers via vc_1. Similar to the diffusion in Pathways 1 and 2, the Na in Pathway 3 also passes through the hexagonal bottleneck. In addition to Pathway 3, the possibility of diffusion along the other inter-layer trajectories that does not proceed through the hexagonal bottleneck, such as the route connecting two Na ions at the Na_2 sites, is also considered. The diffusion in that route encounters a very high barrier of 3 eV, hence Na preferably moves along Pathway 3 when it jumps to the adjacent layers.

3.7   Conclusion

In summary, the density functional theory with the HSE06 and GGA+U methods was utilized to predict the geometrical as well as the electronic structure, the intercalation/deintercalation voltages and the Na diffusion mechanism in NVP. The results of the structures and average voltages in these methods are in good agreement with the previous experimental data. The material is a semiconductor. Similar to the $LiMnPO_4$, Li_2MnSiO_4, and Li_2NiSiO_4 cases, the GGA+U is unfulfilled in handling the polaron problem in NVP. On the other hand, HSE06 was proved to be an effective tool to manage the polaron localization. As a Na vacancy is introduced, the polaron would form at the first nearest neighbor V site to the Na vacancy. Diffusion of Na ions was treated as a process of the polaron-Na vacancy complexes. Diffusion processes inside a Na layer and between the adjacent layers were investigated. Two intra-layer pathways and one inter-layer pathway were explored and the activation energy profiles were calculated. The activation barrier of the intra-layer diffusion is 353 meV, while that of the inter-layer diffusion gains a significantly higher value of 513 meV, respectively. Because of the lower barrier of Pathway 1, as well as Pathway 2, compared with that of Pathway 3, the diffusion of Na inside Na layers is easier than between layers. In preferable pathways, Na always diffuses through the large space of hexagonal bottleneck. A previous study has confirmed that the diffusion on $Li_3V_2(PO_4)_3$ is anisotropic.[55] Hence, the three dimensional diffusion in $Na_3V_2(PO_4)_3$ is an advantage compared to $Li_3V_2(PO_4)_3$.

Chapter IV: NASICON Na$_3$Zr$_2$Si$_2$PO$_{12}$ as an electrolyte material for all-solid state sodium ion batteries

Based on the density functional theory, we have systematically studied the crystal and electronic structures, and diffusion mechanism of the NASICON-type solid electrolytes Na$_3$Zr$_2$Si$_2$PO$_{12}$. Three preferable diffusion pathways are addressed: two inner-chain pathways and one inter-chain pathway. In inner-chain pathways, Na tends to move inside the Na diffusion chain, while in inter-chain pathway, Na moves across the Na diffusion chain. The activation energies for the inner-chain and inter-chain pathways are 230 meV and 260 meV, respectively. The Na vacancy may prefer to diffuse inside the chains due to the lower activation barrier of inner-chain compared to the inter-chain pathways.

Most of the discussion in this section is taken from our manuscript.

4.1 Background

NASICON is one of the promising candidates for applications in solid state electrochemistry where fast ionic conductivity is required. Indeed, The NASICON structure, which is referred to the family of Na$_{1+x}$Zr$_2$Si$_x$P$_{3-x}$O$_{12}$ (0<x<3),[56–61] is famous for its high ionic conductivity. The discovery of the NASICON family has made further development in designing the fast Na$^+$-conductor electrolyte. The

3-D NASICON framework structure enables the material to have good structural stability and fast ion conduction. Hong and Goodenough[49,62] have reported that, the ionic conductivity of $Na_{1+x}Zr_2Si_xP_{3-x}O_{12}$ ($0<x<3$) varies according to the stoichiometry of the NASICON composition. The highest conductivity is obtained in the range of $1.8 < x < 2.2$ where the material possesses a monoclinic C2/c space group. Especially, the conductivities obtained for the composition $Na_3Zr_2Si_2PO_{12}$ (NZSP) [59,63–65] is comparable to the Na β'' alumina.[49]

4.2   Calculation scheme

Here, we investigate the crystal and electronic structure, and the diffusion in NASICON-type electrolyte material NZSP using the GGA method[51]. The space group of NVP is monoclinic C2/c which contains of four formula units (f.u). There are 20 atoms in a f.u of NVP: 3 Na, 2 Zr, 2 Si, 1 P, and 12 O atoms. First, we find the most energetic stable structure by optimizing all possible arrangements of Na ions in the NASICON-type structure of NZSP. The electronic structures of the obtained structure and the defect structure with a vacancy at the Na site were investigated. The diffusion mechanism is explored through the finding of EDPs. The most preferable diffusion pathways then were revealed. The activation energies of the material along the different directions were determined by calculating the activation barriers of EDPs using the NEB[52] method.

All the calculations presented here were carried out using VASP.[53] A $2\times2\times2$ k-point grid was used. The cut-off energy was set at 500eV for generating the plane wave basis set. Both bulk and geometry with one Na vacancy were fully optimized. The optimization calculation is converged if the residual force is less than 10^{-2} eV/Å.

4.3   Crystal structure

$Na_3Zr_2Si_2PO_{12}$ possesses monoclinic C2/c space group as shown in **Fig. 23**. The unit cell consists of four

f.u. There are 20 atoms in a f.u of NZVP: 3 Na, 2 Zr, 1 P, 2 Si, and 12 O atoms. $Na_3Zr_2Si_2PO_{12}$ is a three-dimensional framework created by alternative arranged PO_4 and SiO_4 tetrahedral and ZrO_6 octahedral. Each ZrO_6 octahedra shares its corner with six PO_4 or SiO_4 tetrahedra while each PO_4 or SiO_4 tetrahedra is connected to four ZrO_6 octahedra. This structure creates a "hexagonal bottleneck" built of alternative corner sharing of three ZrO_6 octahedra and three PO_4 or SiO_4 tetrahedral. The shortest diameter of the "hexagonal bottlenecks" is 4.6 Å, which is even bigger by twice the sum of the Na^+ and O^{2-} ionic radii. Such large space enables Na to move through, hence enhancing the conductivity of the material. Especially, we have found that, there are "octagonal bottlenecks" created by alternative corner sharing of four ZrO_6 octahedra and four SiO_4 tetrahedra besides the "hexagonal bottlenecks". This feature makes it much easier for Na to diffuse in the cell. We will have further discussion about the effect of "hexagonal bottleneck" and "octagonal bottlenecks" on Na diffusion in the diffusion mechanism section. There are three different Na sites in the structure: Na_1, Na_2, and Na_3.[49] The position of Na_1, Na_2, and Na_3 are shown in **Fig. 22**. For construction of the material, we considered many Na-vacancy arrangements from the initial structure and then chose the most stable arrangement for further study. The distribution of Na in Na sites in the primitive cell is shown in **Fig. 22a**. In order to obtain the most stable $Na_3Zr_2Si_2PO_{12}$ structure, we have tested many possibilities in which twelve Na occupy four Na_1 sites, four Na_2 sites, and eight Na_3 sites, or in other words, four Na vacancies were located at four Na_1 sites, four Na_2 sites, and eight Na_3 site. There are three groups in which four Na vacancies locate at:

-             Group 1: four Na_1 sites

-             Group 2: four Na_2 sites
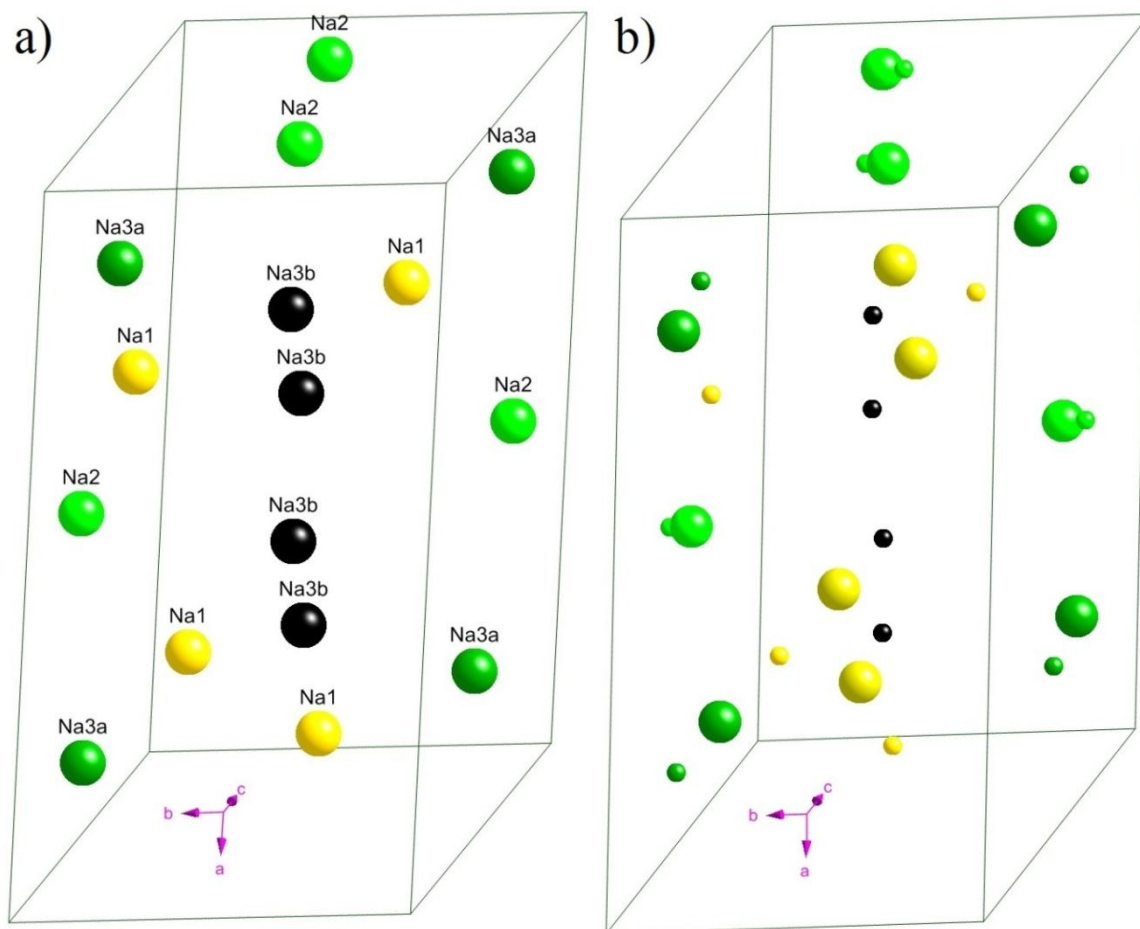
-             Group 3: four sites of eight Na_3 sites

Fig. 22: The position of different Na sites in Na$_3$Zr$_2$Si$_2$PO$_{12}$. Na at the Na$_1$ site are shown by yellow balls, Na at the Na$_2$ site by light green balls, Na$_3$ site by dark green and black balls. a) Original structure. b) Optimized structure. For comparison, the Na in the original structure are shown by small balls, and the Na in the optimized structure are shown by big balls,.

Table 7: Total energy of NVP configurations.

Total energy (eV)	1st (most stable)	2nd	3rd
Group 1			-607.67
Group 2		-.607.90	
Group 3	-608.93		

The total energy of three groups is shown in *Table 7*. According to *Table 7*, the most stable configuration is the Na vacancies locates at four symmetry Na_3 sites while the least stable configuration is the Na vacancies locates at four Na_1 sites. Hence, a formula unit of the most stable $Na_3Zr_2Si_2PO_{12}$ includes one Na at the Na_1 site, one Na at the Na_2 site, and one Na at the Na_3 sites. **Fig. 22b** shows the Na distribution in the optimized cell. For comparison, the Na in the original structure is also presented in small balls with same color. We have found that, while the position of Na_2 site is almost unchanged, that of Na_1 and Na_3 sites may vary.

The obtained structure of $Na_3Zr_2Si_2PO_{12}$ is shown in **Fig. 23**. Similar to $Na_3V_2(PO_4)_3$, $Na_3Zr_2Si_2PO_{12}$ possesses three-dimensional skeletal network of PO_4 tetrahedra sharing their corner with ZrO_6. The calculated lattice parameters are listed in *Table 8*. The calculated parameters obtained are a = 15.801 Å, b = 9.147 Å, and c = 9.245 Å. It can be seen that the optimized lattice parameters are in well agreement with the experiment. The bond distances of Na_1-O, Na_2-O, Na_3-O P-O, Si-O and Zr-O are listed in *Table 9*. We have found that the calculated P-O, and Zr-O bond distances are in accordance with the experiment. In experimental data, the Si-O and P-O bond distances are almost the same. This is

because the structure that the experimentalists proposed was based on the assumption that the Si atoms are ordered in the P positions. Hence, our result of Si-O bond of 1.643 Å, which is in accordance with other experiments,[61,64] is reasonable. Furthermore, since we realized that the Na_3-O bond length is similar to that of Na_1-O, we can rename Na_3 as Na_1. Hence, in our calculation, there are only two types of Na: Na_1 and Na_2. The formation energy calculations indicate that the vacancy at the Na_2 site is approximately 60 meV lower than that at the Na_1 site.

Table 8: The experimental and calculated lattice parameters (Å) in $Na_3Zr_2Si_2PO_{12}$.

	a (Å)	b(Å)	c (Å)
Exp.[49]	15.586	9.029	9.205
Calculation	15.801	9.147	9.245
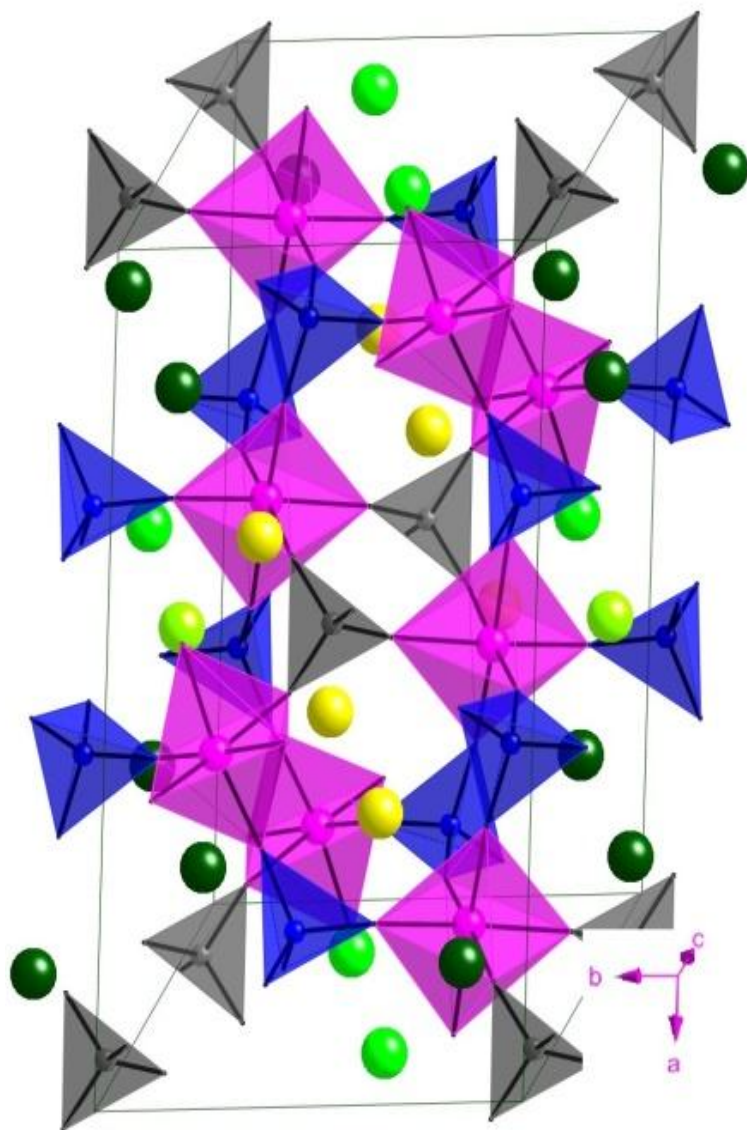
Fig. 23: The crystal structure of Na₃Zr₂Si₂PO₁₂. Na at the Na₁ site are shown by yellow balls, Na at the Na₂ site by light green balls, and Na at the Na₃ site by dark green balls. The Zr octahedra are shown by pink, the Si tetrahedra by blue, and the P tetrahedra by grey.

Table 9: The bond distances (Å) of Na$_1$-O, Na$_2$-O, Na$_3$-O P-O, Si-O and Zr-O in Na$_3$Zr$_2$Si$_2$PO$_{12}$.

	Experiment[49]	Calculation
Na$_1$-O (Å)	2×2.599 2×2.620 2×2.608	2.364 2.369 2.392 2.527 2.533 3.008
Na$_2$-O (Å)	2×2.413 2×2.600 2×2.808 2×2.974	2×2.453 2×2.529 2×2.618 2×2.733
Na$_3$-O (Å)	2.441 2.449 2.478 2.621 2.648 2.772	2.364 2.369 2.392 2.527 2.533 3.008
P-O (Å)	2×1.542 2×1.546	2×1.546 2×1.555
Si-O (Å)	1.543 1.545 1.546	1.636 1.643 1.643

	1.583	1.648
Zr-O	2.055	1.989
	2.077	2.060
	2.096	2.076
	2.104	2.125
	2.137	2.146
	2.142	2.250

4.4   Electronic structure

Fig. 24 illustrates the non spin-polarized DOS of the bulk $Na_3Zr_2Si_2PO_{12}$. The projected DOS on the 3d-states of Zr atoms and the 2p-states of P, Si, and O atoms are also presented. We found that the conduction band is mainly contributed by 2p states of O while the valence band is dominated by 3d states of Zr. The 3d-states of Zr and the 2p-states of O are highly localized. Owing to wide band-gap of 4.6 eV, the material can be considered as an insulator.
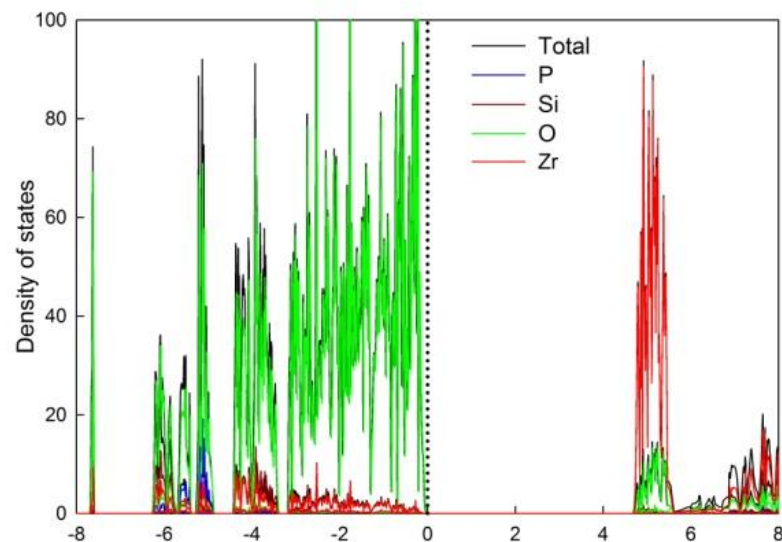
Fig. 24: DOS of the bulk of $Na_3Zr_2Si_2PO_{12}$.

4.5   Diffusion mechanism

When a Na vacancy is introduced into the structure, the neighboring Na ions may jump into the vacant site. In this material, three preferable diffusion pathways are addressed: two inner-chain pathways and one inter-chain pathway.

Fig. 25 shows the diffusion mechanism in inner-chain pathways. The Na vacancy sites are indexed as Na_i (i = A, B, C, D, E, and F). First, we will clarify the diffusion in Pathway 1, which takes place in ($1\overline{2}\overline{2}$) plane. Na diffuses along the path $Na_A \leftrightarrow Na_B \leftrightarrow Na_c \leftrightarrow Na_D$ along the zig-zag line as described in detail as following:

     i)   Process 1:   the Na vacancy diffuses from Na_A to Na_B along [$1\overline{2}2$] direction. The diffusion takes place from the Na_2 to Na_1 site. The diffusion distance is 5.237 Å.

     ii)   Process 2:   the Na vacancy moves from Na_B to Na_C along [$12\overline{2}$] direction. The diffusion distance is 3.322 Å. Both Na_B and Na_C locate at the Na_1 sites.

     iii)   Process 3:   the Na vacancy jumps from Na_C to Na_D along the direction parallel to the Process 1. The Na vacancy diffuses from the Na_1 site to the Na_2 site with a distance of 5.252 Å.

Fig. 26 depicts the activation barrier of Pathway 1. The energy barrier of Process 1 and 3 is 230 meV while that of Process 2 is 65 meV. In Process 1 and 3, Na jumps from the Na_1 site to Na_2 site while in Process 2, Na moves between the same Na_1 sites. This indicates that, the Na diffusion in Process 2 is easier than that in Process 1 and 3. The diffusion trajectory of Pathway 1 is depicted in **Fig. 27**. The Na_A-Na_B (3.7 Å) and Na_B-Na_C (3.9 Å) distances are almost the same. The Na diffusion trajectory of Process 2 is straight, while those for Processes 1 and 3 are parabolic. Therefore, this Na diffusion path in Process 2 is shorter than those in Processes 1 and 3. In Process 1 and 3, Na migrates through the "hexagonal bottleneck" while Na travels easily through the large "octagonal bottleneck" in Process 2.
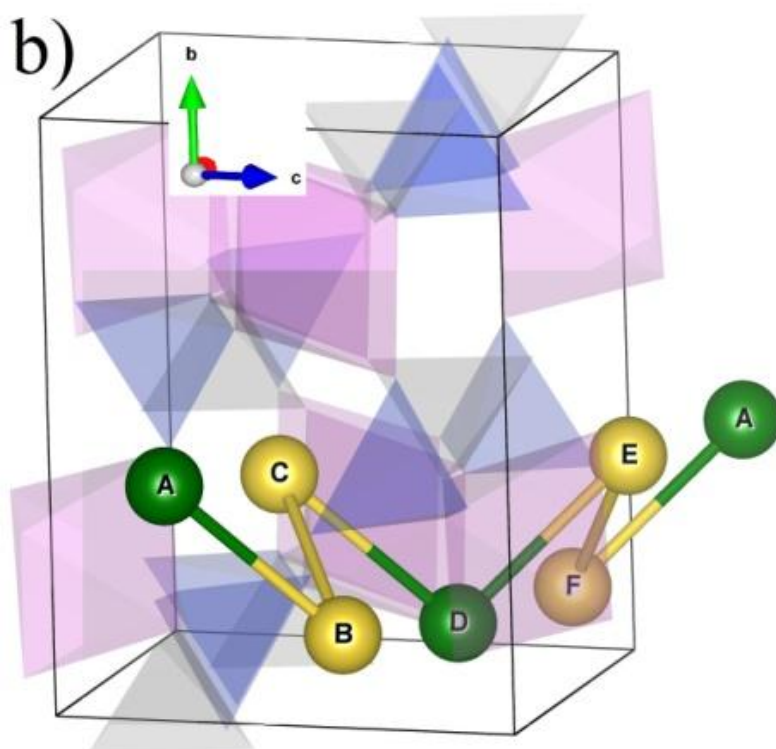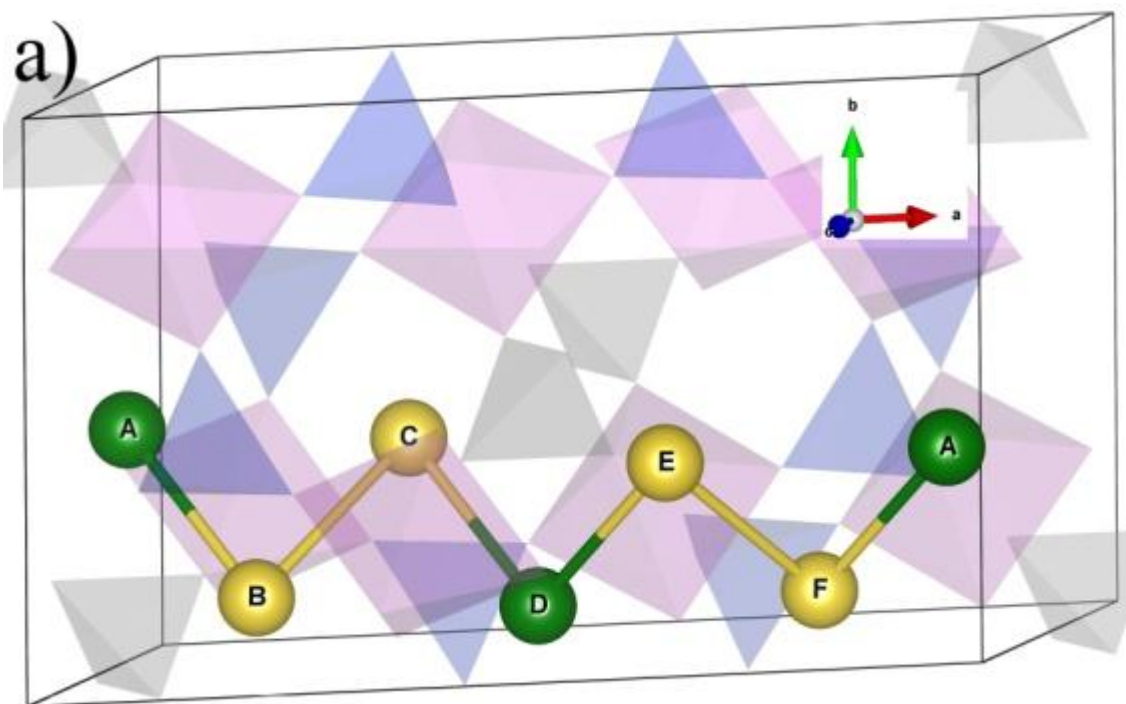
Fig. 25: Schematic of Pathway 1 and 2. The Na at Na1 site are shown in yellow balls while the Na at Na2 site are shown in green balls. a) c-direction view. b) side view
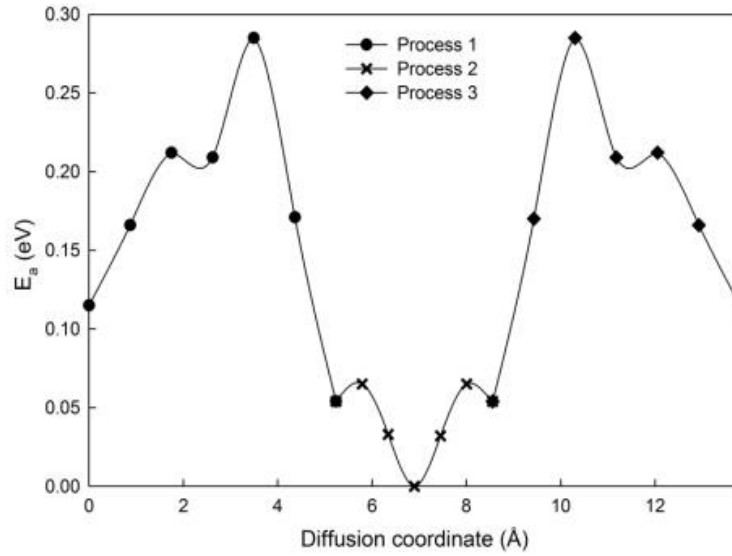
Fig. 26: Activation energies of the Na vacancy diffusion along Pathway 1. The circle, cross, and diamond symbols represent the activation energy profile of the processes 1, 2, and 3, respectively.

Hence, as seen in **Fig. 26**, E_a of Process 2 is lower than that of Process 1 and 3. The images of the diffusion through "hexagonal bottleneck" and "octagonal bottleneck" are shown in **Fig. 28**. The "octagonal bottleneck" is created by alternatively arranged four ZrO_6 octahedra and four SiO_6 tetrahedra sharing their corners. Four ZrO_6 octahedra lie on $(31\bar{1})$ plane and four SiO_4 tetrahedra stand on (521) plane causing a high symmetry environment as depicted in **Fig. 28c**. Hence, when a Na vacancy is introduced at Na_B (Na_C), the Na at Na_C (Na_B) tends to move to the middle point between Na_B and Na_C. Therefore, the activation profile of Process 2 is as described in **Fig. 26.**

Pathway 2 is proceeded along $Na_D \leftrightarrow Na_E \leftrightarrow Na_F \leftrightarrow Na_A$ route lying on the $(12\bar{2})$ plane as shown in **Fig. 25.** The diffusion mechanism, as well as activation barrier, of the elementary processes in Pathway 2 is similar to those in Pathway 1. For more detail:

iv)   Process 4: the Na vacancy moves from Na_D to Na_E along [122] direction. The diffusion distance and activation energy are similar to those in Process 1.

v)   Process 5: the Na vacancy migrates from Na_E to Na_F along $[\bar{1}22]$ direction. The diffusion mechanism is similar to Process 2.

vi)   Process 6: the Na vacancy jumps from Na_F to Na_A along the direction parallel to the Process 4. The characteristic of the diffusion is identical to Process 3.

As seen in **Fig. 25b**, the diffusion plane of Pathway 2 is perpendicular to that of Pathway 1. Na vacancy migrates along the chain in *a*- direction in Pathways 1 and 2. Thanks for the good stability of P-O and Si-O bonds, the $Zr_2Si_2PO_{12}$ frameworks retain its structure during the Na diffusion.

Next, we would like to explain how Na vacancy behaves in Pathway 3. We have defined the Na diffusion chain, which is indicated by surrounded dash line in **Fig. 29.** Since in Pathway 1 and 2, the Na vacancy migrates inside a Na layer, those pathways are named as an inner-chain pathway. In Pathway 3, Na jumps from one Na diffusion chain to the other chain. Hence, the pathway is named as an inter-chain pathway which is shown by red arrow in **Fig. 29**. We have investigated the inter-chain pathway $Na_F \leftrightarrow Na_C$ (or $Na_B \leftrightarrow Na_E$) and find that Na still has to diffuse through the "hexagonal bottleneck". The activation barrier for this pathway is 260 meV as depicted in **Fig. 30**. In addition, although we also studied other pathways such as $Na_B \leftrightarrow Na_F$, the Na has to climb up a higher energy barrier of 460 meV because there is no "hexagonal bottleneck" or "octagonal bottleneck" appeared along this pathway. Hence, the most preferable path to connect Na diffusion chains is the Pathway 3.
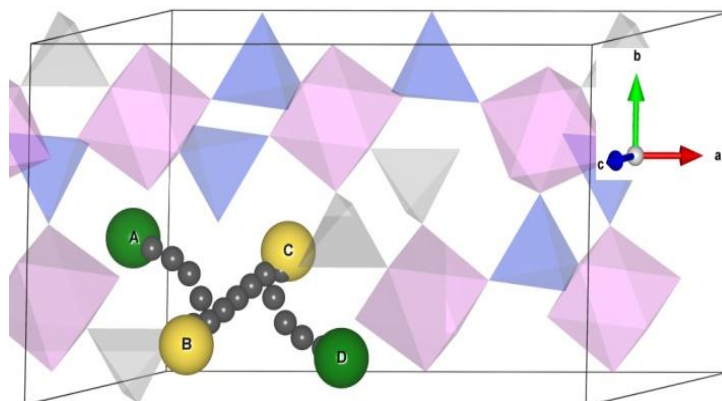

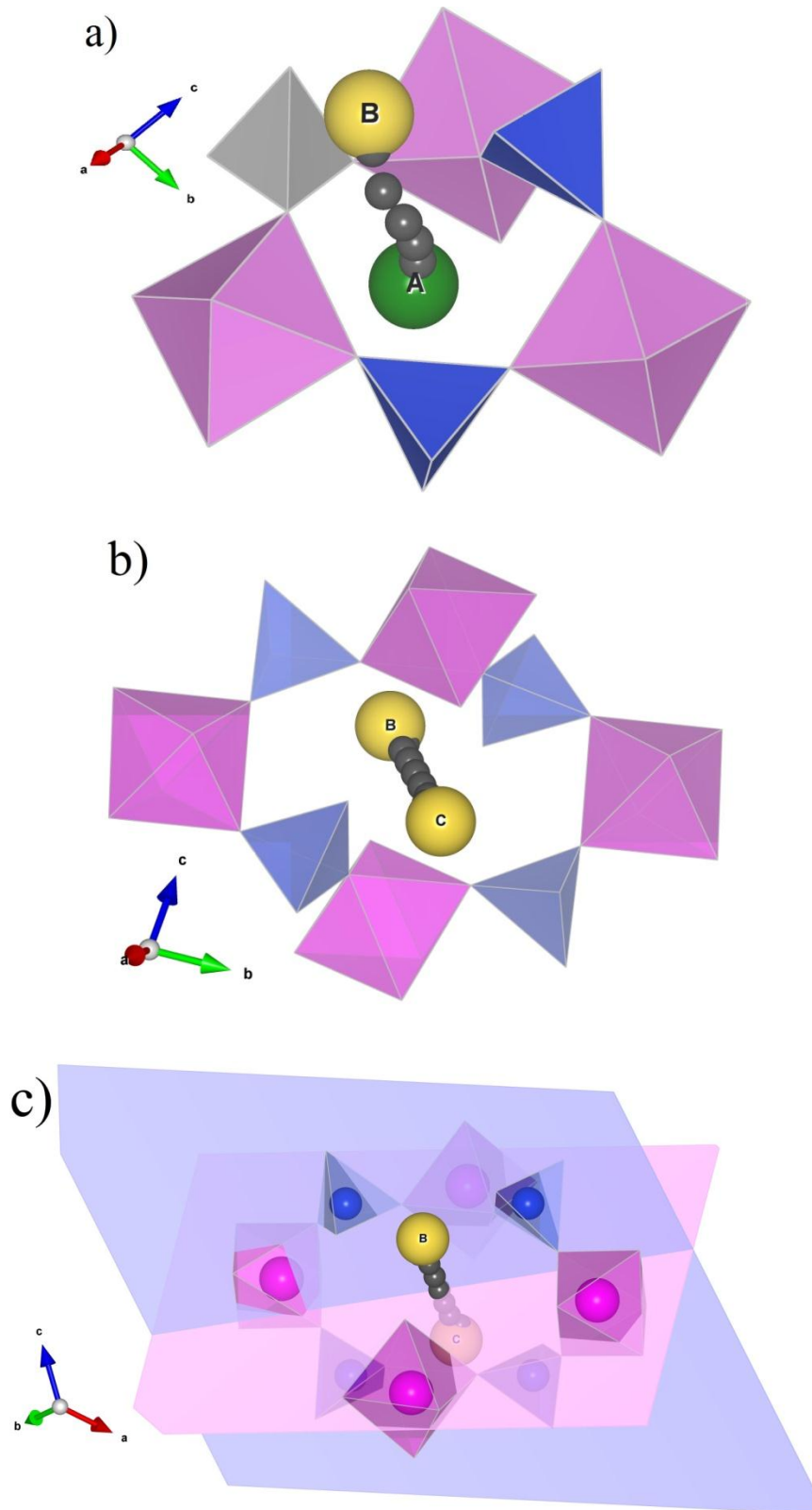**Fig. 27: Diffusion orbit of Pathway 1. Intermediate Na are shown in deep grey balls.**

Fig. 28: Schematic of Na diffusion through hexagonal bottlenecks and octagonal bottleneck.

a) Process 1 b) Process 2 c) Process 2 with planes. The ZrO_6 octahedra and SiO_4 tetrahedra planes

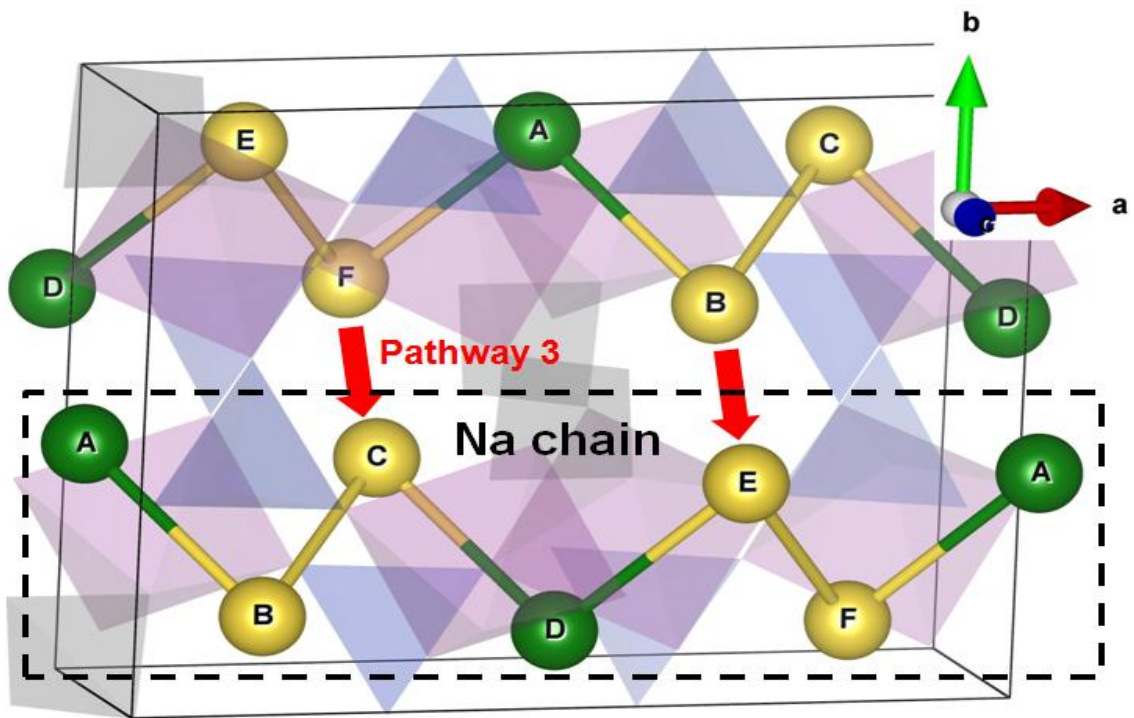**are shown in pink and blue, respectively.**

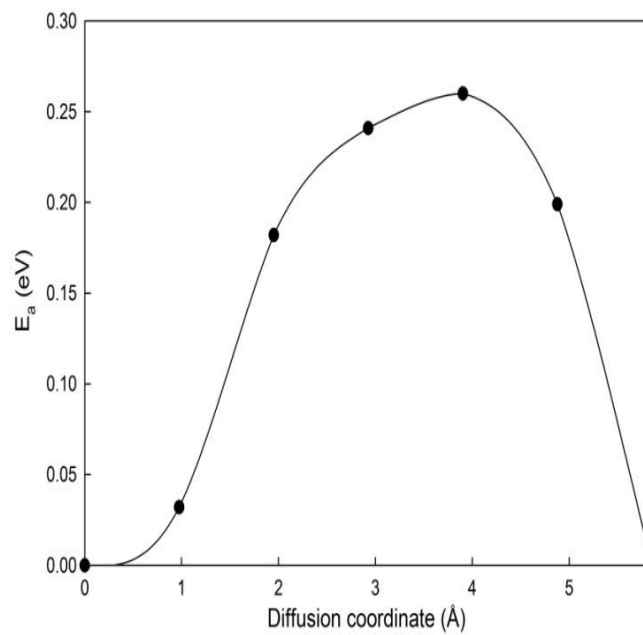**Fig. 29: Schematic of Pathway 3. The Na chain is indicated by surrounded dash line.**

Fig. 30: Activation energies of the Na vacancy diffusion along Pathway 3.

4.6   Conclusion

We have investigated the geometrical and the electronic structure, and the Na diffusion mechanism in $Na_3Zr_2Si_2PO_{12}$ based on the density functional theory. The obtained lattice parameters and bond lengths of the structure are in accordance with the experiment. Two Na sites were found: Na_1 and Na_2. The three dimensional diffusion is confirmed in this study. Furthermore, two inner-chain pathways and one inter-chain pathway were examined. The activation barriers for the inner-chain and inter-chain pathways are 230 meV and 260 meV, respectively. The Na vacancy may prefer to diffuse inside chains due to the lower activation barrier of inner-chain compared to inter-chain pathways. In the processes in which Na moves between the Na_1 site to Na_2 site, Na has to diffuse through the "hexagonal bottleneck". But in processes in which Na moves between the same Na_1 sites, Na moves easily across the "octagonal bottleneck".

Chapter V: NVP/NZSP interface of NASICON-based all-solid state sodium ion batteries

Based on the density functional theory, the crystal and electronic structures, and diffusion mechanism through the NVP/NZSP interface are investigated. The attachment of the NVP/NZSP interface is found to be more preferable along *a* direction. Most bonds at the interface are saturated. DOS of the interface exhibits the characteristic of a typical interface. Two possible diffusion channels through the interface were addressed.

5.1   Background

Recently, the all solid-state battery using $Na_3V_2(PO_4)_3$ (NVP) as electrode and $Na_3Zr_2Si_2PO_{12}$ as electrolyte is attracting attention as a high performance and low cost battery.[66,67] The NASICON-type $Na_3V_2(PO_4)_3$ electrode and $Na_3Zr_2Si_2PO_{12}$ electrolyte are crucially important by providing good stability and high ionic conductivity as discussed in Chapter III and IV. Since NVP and NZSP have the same NASICON structure and the lattice mismatch between them is about 3%, it is possible to study the NVP/NZSP/NVP cell theoretically and experimentally.

Noguchi *et al.*[67] was the first who fabricated the all solid-state symmetric NVP/NASICON/NVP sodium-ion cell by a combination of screen printing and hot pressing. The fabricated symmetric cell was examined at room temperature and offered a relatively flat discharge profile at the average discharge voltage of 1.8 V vs. Na. The first specific capacity was about 68 mAh g^{-1} which is 80% of the discharge capacity for the equivalent liquid symmetric cell, and 58% of the NVP theoretical capacity. According to their study, the cycle performance of the all solid-state symmetric cell can be significantly improved by decreasing the internal porosity of the NASICON solid electrolyte as well as by precise control of NVP/NASICON interface. It is believed that the development of sodium-ion all solid-state symmetric cells is very advantageous from a commercial standpoint. Such cells exhibit excellent safety, acceptable cost and simplicity of operation because the as-fabricated batteries can be charged in either direction. Lalere *et al.*[66] studied the all-solid state symmetric monolithic sodium ion battery NVP/NASICON/NVP operating at 200 $^{\circ}$C. The battery operates at 1.8 V with 85% of the theoretical capacity attained at C/10 with satisfactory capacity retention, for an overall energy density of 1.87×10^{-3} W h cm^{-2} and a capacity of 1.04 mA h cm^{-2}. To the best of our knowledge, there is still lack of theoretical study of NVP/NZSP/NVP cell.

5.2   Calculation scheme

In this chapter, we investigate the crystal and electronic structure, and the diffusion through NVP/NZSP interface using the GGA method[51]. For comparison, the GGA+U and HSE06 method will be used. [27,51] First, we find the most energetic stable structure by optimizing many possible configurations of the NVP/NZSP interface. In order to assemble the cathode NVP and electrolyte NZSP together, we have used the following configuration:

5 Å Vacuum + 2NVP + Vacuum + 2NZSP + 5 Å Vacuum
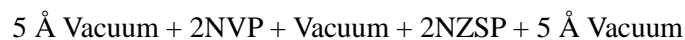
where 5 Å vacuum was attached to maintain the periodic properties. In addition, we have terminated the outermost oxygen by hydrogen to avoid any unphysical magnetism in the system due to the dangling

bond of the oxygen. The electronic structures of the obtained structure and the defect structure with a vacancy at the Na site were investigated. The diffusion mechanism is explored through the finding of EDPs. The most preferable diffusion pathways then were revealed. The activation energies of the material along the different directions were determined by calculating the activation barriers of EDPs using the NEB[52] method.

All the calculations presented here were carried out using VASP.[53] A $1\times1\times1$ k-point grid was used. The cut-off energy was set at 500eV for generating the plane wave basis set. Both bulk and geometry with one Na vacancy were fully optimized. The optimization calculation is converged if the residual force is less than 10^{-2} eV/Å.
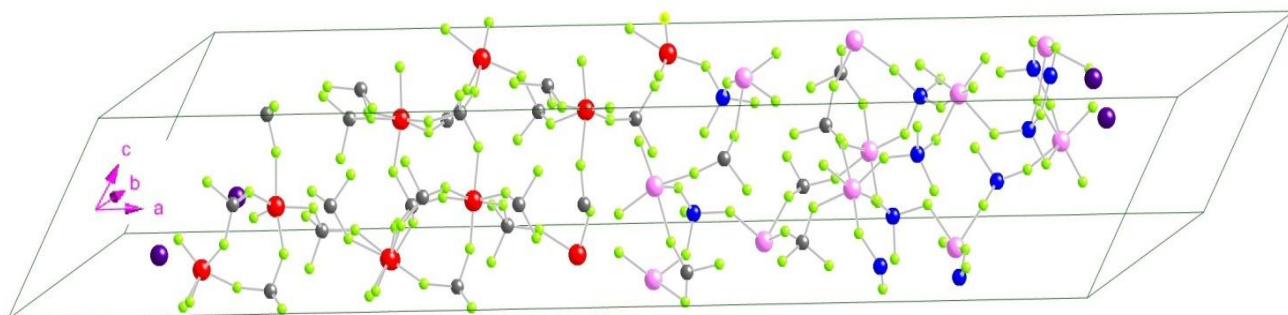
5.3   Crystal structure

Fig. 31: The crystal structure of NVP/NZSP interface. V, Zr, P, Si, H, and O atoms are shown by red, pink, gray, blue, violet, and green balls, respectively.

The optimized structure of the NVP/NZSP interface is shown in **Fig. 31**. The attachment is made along a direction. The lattice parameters obtained are a = 50.518 Å, b = 8.839 Å, c = 8.839 Å; and the angle between them are α = 60.258°, β = 59.607°, γ = 59.607°. It is found that as far as we go from the NVP/NZSP interface, the bond is very similar to the bond in bulk of NVP or NZSP. In NVP part, the

average bond length of P-O and V-O are 1.54 Å and 2.00 Å, respectively. In NZSP part, the average

bond length of P-O, Si-O, and Zr-O are 1.55 Å, 1.64 Å, and 2.10 Å, respectively. Near the interface,

Zr-O bond is slightly elongated from 2.10 Å to 2.20 Å (or 2.30 Å). Also, the average V-O bond length at

the interface slightly changes from 2.00 Å to 1.90 Å. In bulk, there are four neighboring O atoms around

P atom within 2 Å of boundary, while at interface, there is one P atom having only three neighboring O

atoms within 2 Å of boundary. The Si-O bond at the interface is almost similar to that in bulk. Although

some bonds at the edge of the electrode and electrolyte are not saturated, the V-O, P-O and Zr-O bonds

are nearly neutralized at the interface.

As seen in **Fig. 32**, H1 is attached to O1, and H2 is attached to O2. Both O1 and O2 are connected

to V atoms. As depicted in **Fig. 33**, H3 is connected to O3, and H4 is attached to O4. Both O3 and O4

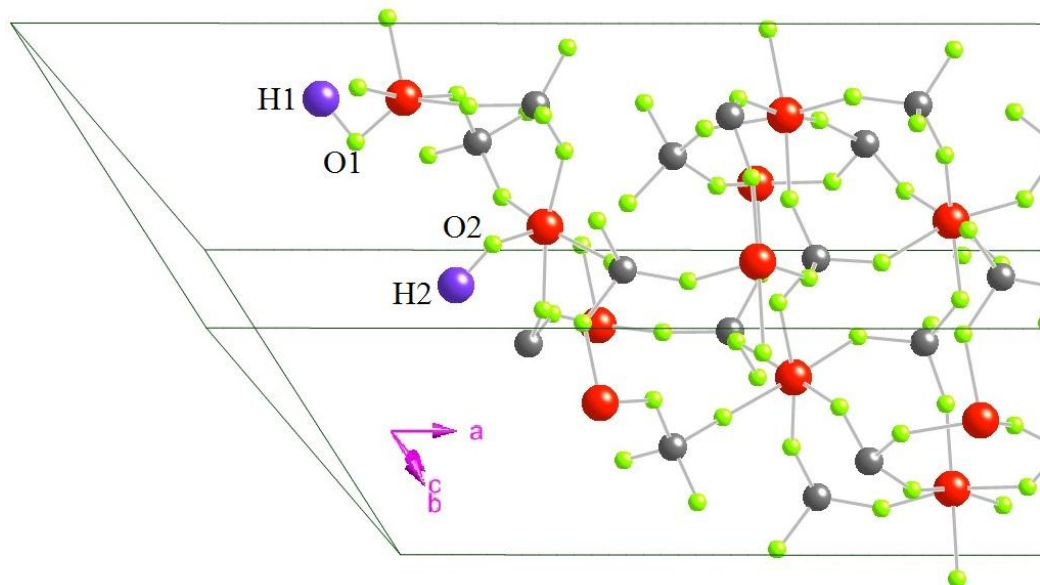are connected to Zr atoms. The average H-O bond length obtained is about 1 Å.

Fig. 32: The crystal structure at NVP termination. V, P, H, and O atoms are shown by red,
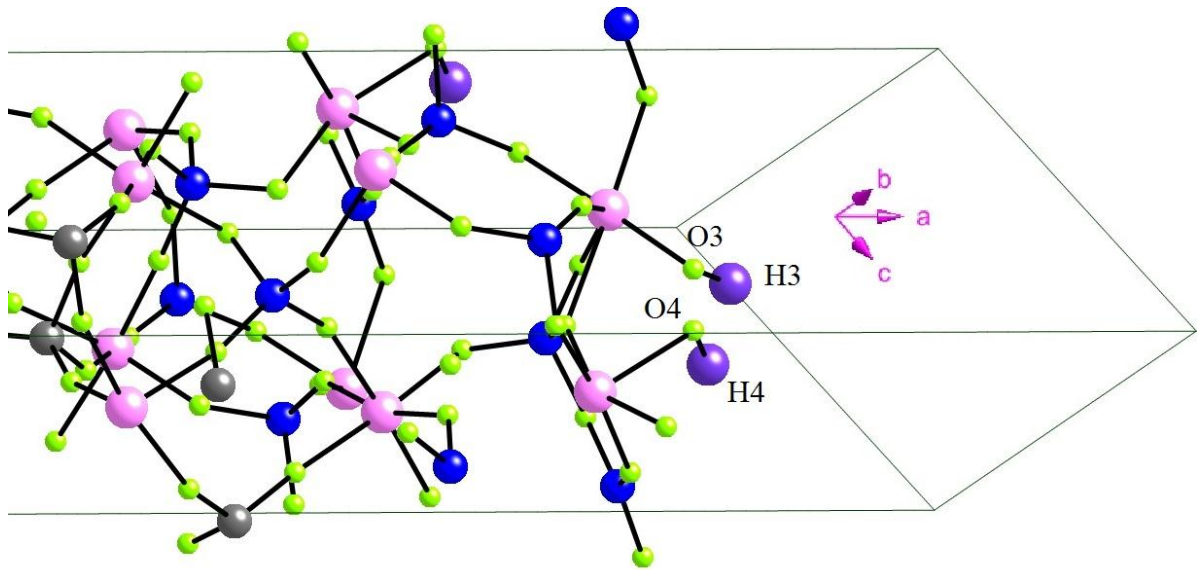
pink, gray, violet, and green balls, respectively.

Fig. 33: The crystal structure at NZSP termination. Zr, P, Si, H, and O atoms are shown by pink, gray, blue, violet, and green balls, respectively.
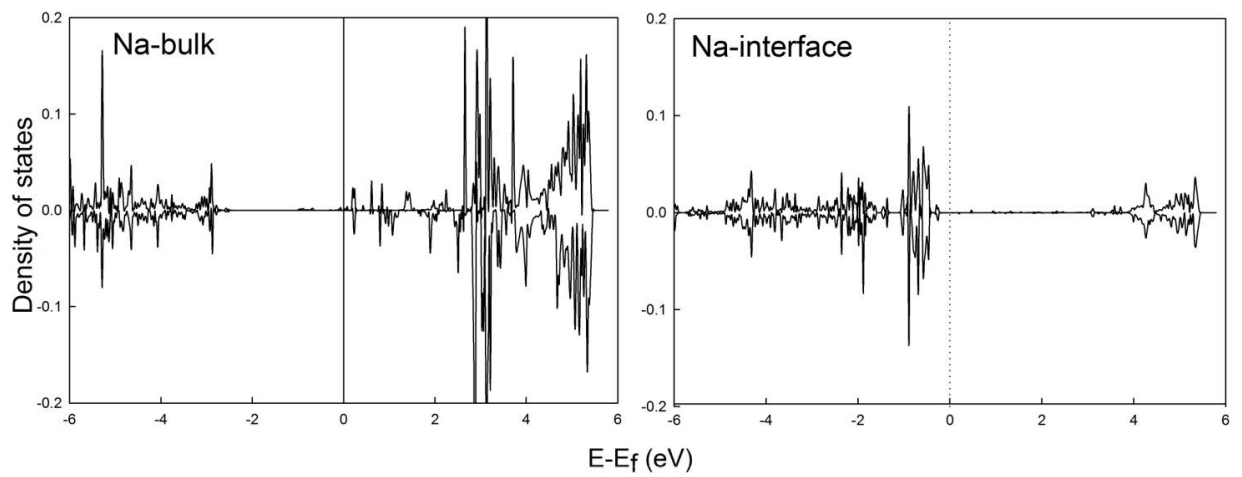
5.4   Electronic structure

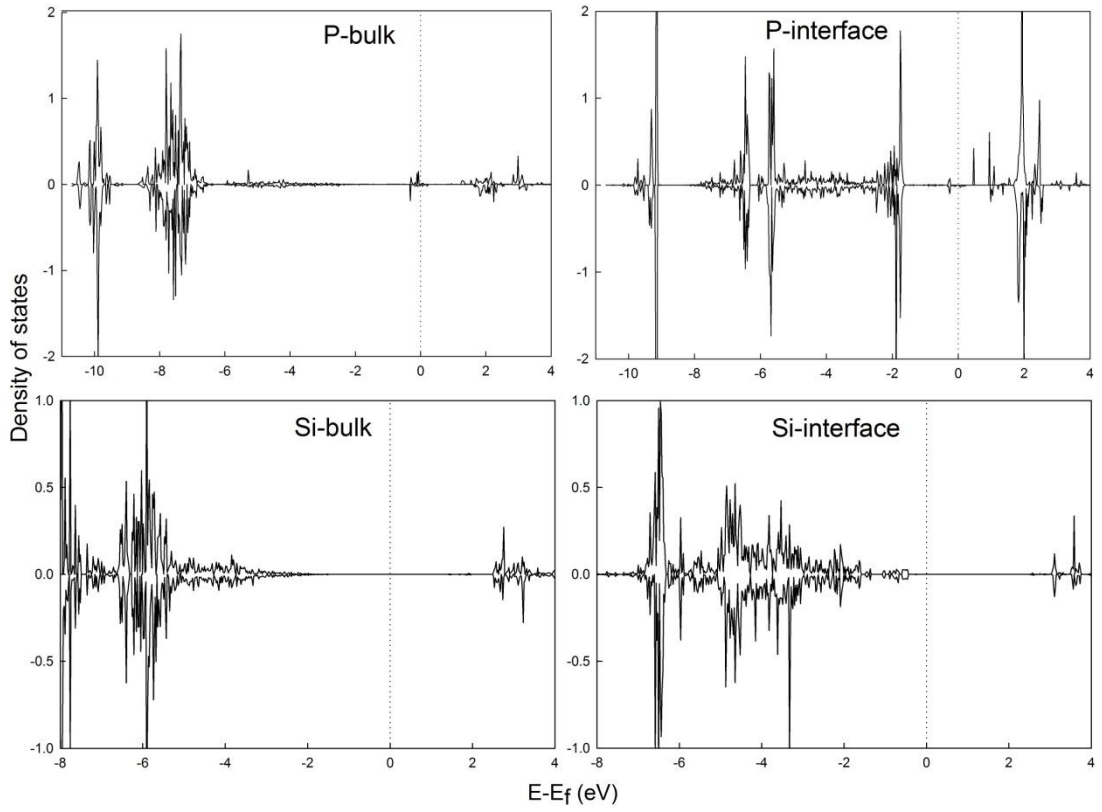**Fig. 34: Antiferromagnetic DOS of Na in bulk and interface.**

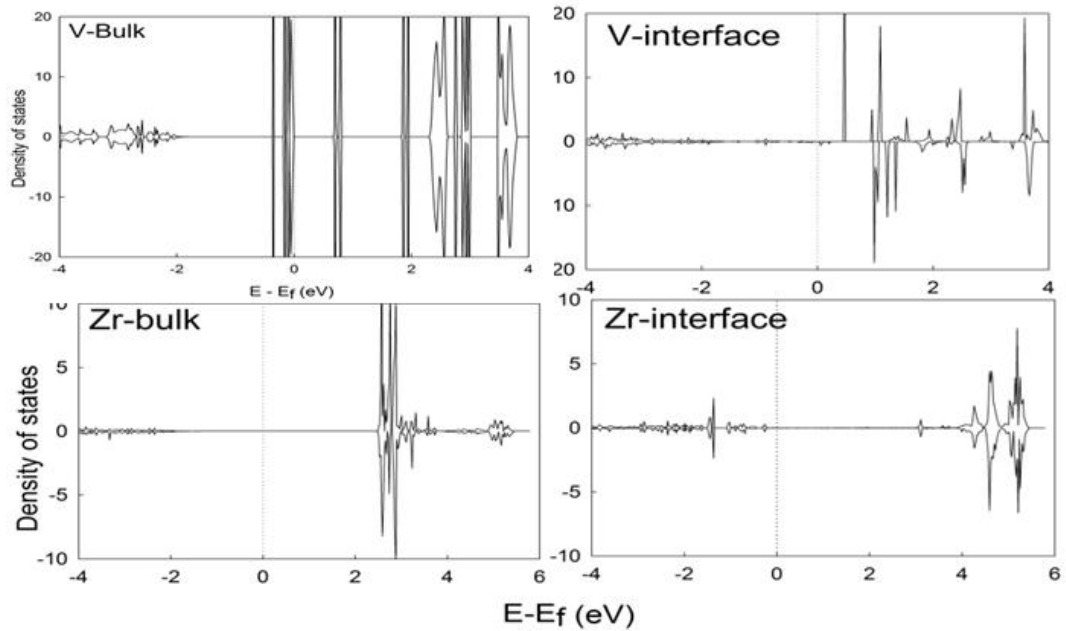**Fig. 35: Antiferromagnetic DOS of P and Si in bulk and interface.**

Fig. 36: Antiferromagnetic DOS of V and Zr in bulk and interface.
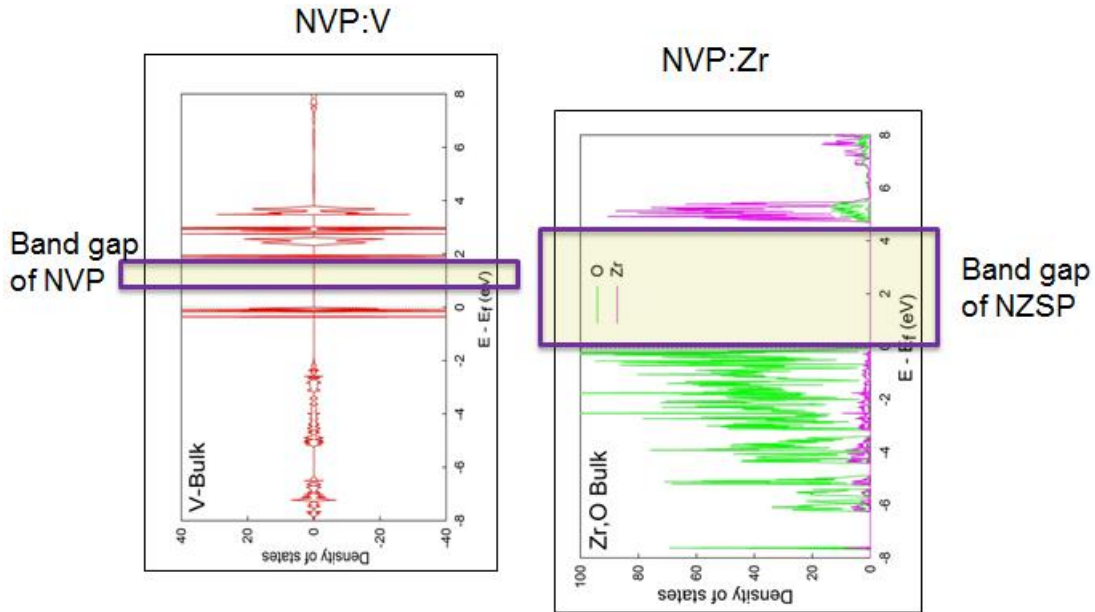
69

Fig. 37: Electrochemical window of NVP and NZSP

In order to understand the electronic structure of the material, the antiferromagnetic DOS of all atoms in bulk and interface are shown. From **Fig. 34**, it is found that the DOS of Na at exited states in bulk are higher and more broaden than that at interface. The occupied levels of the DOS of Si, V, and Zr at the interface tend to slightly shift to higher energy regions, as shown in **Fig. 35** and **Fig. 36**, particularly DOS at unoccupied levels of P becomes bigger. **Fig. 37** shows the wide electrochemical window of NZSP compare to that of NVP.

5.5　　Conclusion

The results of the crystal and electronic structures, and diffusion mechanism of the NVP/NZSP interface are found. The attachment of the NVP/NZSP interface is more preferable along *a* direction. Most bonds at the interface are saturated. DOS of the interface exhibits the characteristic of a good interface.

Chapter VI: Summary

In summary, the NASICON-type materials for the cathode and electrolyte, as well as the cathode/electrolyte interface, of the all-solid-state sodium ion batteries are investigated by using the first principles method. The crystal and electronic structures and the diffusion mechanism of Na ions in the cathode NVP and electrolyte NZSP are revealed. The lattice parameters obtained are in agreement with experiments. The materials are insulators with large band-gap. In NVP, when a Na vacancy is introduced in the material, a small polaron would form around a V site near the vacancy. Our calculation shows that, HSE06 is more appropriate than GGA+U in dealing with polaron problem. During diffusion, the Na vacancy movement will be accompanied by the migration of the polaron. Three most preferable diffusion pathways are addressed: two intra-layer pathways (Pathway 1 and Pathway 2) and one inter-layer pathway (Pathway 3). In Pathway 1, there are four elementary processes: two crossing processes C_1 and C_2, one parallel process P and one single diffusion process S. The activation barriers for P, C1, S, and C_2 processes are 283, 137, 288, and 353 meV, respectively. Pathway 1 and 2 were named as "intra-layer" pathways because in Pathway 1 and 2, Na diffuses within Na diffusion layer. Pathway 3, is one of that called the "inter-layer" pathway because it connects the Na layers via intrinsic vacancy sites. The activation energy of this Pathway is 513 meV. The three dimensional diffusion in $Na_3V_2(PO_4)_3$ is an advantage compared to $Li_3V_2(PO_4)_3$. Having NASICON structure, NZSP has not only "hexagonal bottlenecks" but also "tetragonal bottlenecks". During diffusion, Na should move through such large bottlenecks. In this material, three different diffusion pathways are found: two inner-chain

71

pathways (Pathway 1 and Pathway 2) and one inter-chain pathway (Pathway 3). There are three elementary processes in Pathway 1: Process 1, 2, and 3. The energy barrier of Process 1 and 3 is 230 meV while that of Process 2 is as low as 65 meV. In Process 1 and 3, Na moves through the "hexagonal bottlenecks" while in Process 2, Na passes through the wide "octagonal bottlenecks". Hence, it is easier for Na to diffuse in Process 2 than in Process 1 and 3. Pathway 2 has the same diffusion mechanism as Pathway 1. Pathway 1 and 2 were named as "inner-chain" pathways because in Pathway 1 and 2, Na diffuses within Na diffusion chain. In Pathway 3, Na jumps from one Na diffusion chain to the other chain. Hence, Pathway 3 was named as "inter-chain" pathway. The activation barrier for this pathway is 260 meV. Therefore, the three dimensional diffusion with low activation barriers is confirmed for NZSP. For the NVP/NZSP interface, the attachment is more preferable along a direction. Most bonds at the interface are saturated. DOS of the interface exhibits the characteristic of a good interface. I hope that my study will give a new insight about the structure and Na diffusion mechanism in SIBs and encourage the experimentalists to perform new study in this field.

References

1   D. Larcher and J.-M. Tarascon, *Nat. Chem.*, 2015, **7**, 19–29.

2   N. S. Lewis, *MRS Bull.*, 2007, **32**, 808–820.

3   B. Dunn, H. Kamath and J.-M. Tarascon, *Science*, 2011, **334**, 928–935.

4   J.-M. Tarascon, *Nat. Chem.*, 2010, **2**, 510–510.

5   J. B. Goodenough and Y. Kim, *Chem. Mater.*, 2010, **22**, 587–603.

6   V. A. Dinh, J. Nara and T. Ohno, *Appl. Phys. Express*, 2012, **5**, 045801.

7   K. M. Bui, V. A. Dinh and T. Ohno, *J. Phys. Conf. Ser.*, 2013, **454**, 012061.

8   K. M. Bui, V. A. Dinh and T. Ohno, *Appl. Phys. Express*, 2012, **5**, 125802.

9   D. M. Duong, V. A. Dinh and T. Ohno, *Appl. Phys. Express*, 2013, **6**, 115801.

10   *Practical Handbook of Physical Properties of Rocks & Minerals*, CRC Press, Boca Raton, Fla, 1 edition., 1988.

11   N. Yabuuchi, K. Kubota, M. Dahbi and S. Komaba, *Chem. Rev.*, 2014, **114**, 11636–11682.

12   V. Palomares, P. Serras, I. Villaluenga, K. B. Hueso, J. Carretero-González and T. Rojo, *Energy Environ. Sci.*, 2012, **5**, 5884–5901.

13   S. P. Ong, V. L. Chevrier, G. Hautier, A. Jain, C. Moore, S. Kim, X. Ma and G. Ceder, *Energy Environ. Sci.*, 2011, **4**, 3680–3688.

14   J.-J. Ding, Y.-N. Zhou, Q. Sun and Z.-W. Fu, *Electrochem. Commun.*, 2012, **22**, 85–88.

15   R. Berthelot, D. Carlier and C. Delmas, *Nat. Mater.*, 2011, **10**, 74–80.

16   S.-M. Oh, S.-T. Myung, J. Hassoun, B. Scrosati and Y.-K. Sun, *Electrochem. Commun.*, 2012, **22**, 149–152.

17   H. Zhuo, X. Wang, A. Tang, Z. Liu, S. Gamboa and P. J. Sebastian, *J. Power Sources*, 2006, **160**, 698–703.

18   J.-M. Tarascon and M. Armand, *Nature*, 2001, **414**, 359–367.

19   K. Takada, *Acta Mater.*, 2013, **61**, 759–770.

20   K. M. Bui, V. A. Dinh, S. Okada and T. Ohno, *Phys Chem Chem Phys*, 2015, **17**, 30433–30439.

21   P. Hohenberg and W. Kohn, *Phys. Rev.*, 1964, **136**, B864–B871.

22   W. Kohn, *Rev. Mod. Phys.*, 1999, **71**, 1253–1266.

23   J. Harris and R. O. Jones, *J. Phys. F Met. Phys.*, 1974, **4**, 1170.

24   D. C. Langreth and J. P. Perdew, *Solid State Commun.*, 1975, **17**, 1425–1429.

25   A. D. Becke, *Phys. Rev. A*, 1988, **38**, 3098–3100.

26   J. P. Perdew, J. A. Chevary, S. H. Vosko, K. A. Jackson, M. R. Pederson, D. J. Singh and C. Fiolhais, *Phys. Rev. B*, 1992, **46**, 6671–6687.

27   J. P. Perdew, K. Burke and M. Ernzerhof, *Phys. Rev. Lett.*, 1996, **77**, 3865–3868.

28   V. I. Anisimov, F. Aryasetiawan and A. I. Lichtenstein, *J. Phys. Condens. Matter*, 1997, **9**, 767.

29   V. I. Anisimov, J. Zaanen and O. K. Andersen, *Phys. Rev. B*, 1991, **44**, 943–954.

30   V. I. Anisimov and O. Gunnarsson, *Phys. Rev. B*, 1991, **43**, 7570–7574.

31   I. V. Solovyev, P. H. Dederichs and V. I. Anisimov, *Phys. Rev. B*, 1994, **50**, 16861–16871.

32   S. Park, B. Lee, S. H. Jeon and S. Han, *Curr. Appl. Phys.*, 2011, **11**, S337–S340.

33   M. D. Johannes, K. Hoang, J. L. Allen and K. Gaskell, *Phys. Rev. B*, 2012, **85**, 115106.

34   V. A. Dinh, J. Nara and T. Ohno, 2012.

35   M. C. Payne, M. P. Teter, D. C. Allan, T. A. Arias and J. D. Joannopoulos, *Rev. Mod. Phys.*, 1992, **64**, 1045–1097.

36   H. J. Monkhorst and J. D. Pack, *Phys. Rev. B*, 1976, **13**, 5188–5192.

37   D. Sheppard, R. Terrell and G. Henkelman, *J. Chem. Phys.*, 2008, **128**, 134106.

38   G. Pistoia, *Lithium-Ion Batteries: Advances and Applications*, Newnes, 2013.

39   J. Gopalakrishnan and K. K. Rangan, *Chem. Mater.*, 1992, **4**, 745–747.

40   Y. Uebo, T. Kiyabu, S. Okada and J. Yamaki, *Rep. Inst. Adv. Mater. Study Kyushu Univ.*, 2002, **16**, 1–5.

41   K. Du, H. Guo, G. Hu, Z. Peng and Y. Cao, *J. Power Sources*, 2013, **223**, 284–288.

42   M. Pivko, I. Arcon, M. Bele, R. Dominko and M. Gaberscek, *J. Power Sources*, 2012, **216**, 145–151.

43   J. Kang, S. Baek, V. Mathew, J. Gim, J. Song, H. Park, E. Chae, A. K. Rai and J. Kim, *J. Mater. Chem.*, 2012, **22**, 20857–20860.

44   Z. Jian, L. Zhao, H. Pan, Y.-S. Hu, H. Li, W. Chen and L. Chen, *Electrochem. Commun.*, 2012, **14**, 86–89.

45   Z. Jian, W. Han, X. Lu, H. Yang, Y.-S. Hu, J. Zhou, Z. Zhou, J. Li, W. Chen, D. Chen and L. Chen, *Adv. Energy Mater.*, 2013, **3**, 156–160.

46   K. Saravanan, C. W. Mason, A. Rudola, K. H. Wong and P. Balaya, *Adv. Energy Mater.*, 2013, **3**, 444–450.

47   C. Zhu, K. Song, P. A. van Aken, J. Maier and Y. Yu, *Nano Lett.*, 2014, **14**, 2175–2180.

48   N. Böckenfeld and A. Balducci, *J. Solid State Electrochem.*, 2013, **18**, 959–964.

49   H. .-P. Hong, *Mater. Res. Bull.*, 1976, **11**, 173–182.

50   K. M. Bui, 2013.

51   K. Hummer, J. Harl and G. Kresse, *Phys. Rev. B*, 2009, **80**, 115205.

52   G. Henkelman and H. Jónsson, *J. Chem. Phys.*, 2000, **113**, 9978–9985.

53   G. Kresse and J. Hafner, *Phys. Rev. B*, 1993, **47**, 558–561.

54   I. A. Courtney, J. S. Tse, O. Mao, J. Hafner and J. R. Dahn, *Phys. Rev. B*, 1998, **58**, 15583–15588.

55   S. Lee and S. S. Park, *J. Phys. Chem. C*, 2012, **116**, 25190–25197.

56   R. M. Hazen, L. W. Finger, D. K. Agrawal, H. A. McKinstry and A. J. Perrotta, *J. Mater. Res.*, 1987, **2**, 329–337.

57   J. P. Boilot, G. Collin and P. Colomban, *Mater. Res. Bull.*, 1987, **22**, 669–676.

58   J. P. Boilot, G. Collin and P. Colomban, *J. Solid State Chem.*, 1988, **73**, 160–171.

59   O. Bohnke, S. Ronchetti and D. Mazza, *Solid State Ion.*, 1999, **122**, 127–136.

60   U. Warhus, J. Maier and A. Rabenau, *J. Solid State Chem.*, 1988, **72**, 113–125.

61   D. T. Qui, J. J. Capponi, J. C. Joubert and R. D. Shannon, *J. Solid State Chem. Fr.*, 1981, **39**, 219–229.

62   J. B. Goodenough, H. Y.-P. Hong and J. A. Kafalas, *Mater. Res. Bull.*, 1976, **11**, 203–220.

63   N. G. Bukun, *Ionics*, 1996, **2**, 63–68.

64   P. P. Kumar and S. Yashonath, *J. Phys. Chem. B*, 2002, **106**, 7081–7089.

65   M. L. Di Vona, E. Traversa and S. Licoccia, *Chem. Mater.*, 2001, **13**, 141–144.

66   F. Lalère, J. B. Leriche, M. Courty, S. Boulineau, V. Viallet, C. Masquelier and V. Seznec, *J. Power Sources*, 2014, **247**, 975–980.

67   Y. Noguchi, E. Kobayashi, L. S. Plashnitsa, S. Okada and J. Yamaki, *Electrochimica Acta*, 2013, **101**, 59–65.